J. Fluid Mech. (2000), *vol.* 405, *pp.* 79–110. Printed in the United Kingdom

Marangoni convection. Part 1. A cavity with differentially heated sidewalls

By M. HAMED AND J. M. FLORYAN

Department of Mechanical and Materials Engineering,
The University of Western Ontario, London, Ontario, N5A 5B9, Canada

(Received 6 October 1997 and in revised form 6 October 1999)

Marangoni convection in a cavity with differentially heated sidewalls has been investigated. The analysis includes the complete effects of interface deformation. The results determined for large Biot and zero Marangoni (zero Prandtl) numbers show that steady convection may exist for Reynolds numbers Re larger than, and for capillary numbers Ca and cavity lengths L smaller than, certain critical values. The main factor limiting the existence of steady convection involves the interface becoming tangential to the hot wall at the contact point (tangency condition). Unsteady analysis shows that the tangency condition defines the limit point for the system; its violation is most likely to lead to the formation of a dry spot at the hot wall. The critical values of Re, Ca, and L are mutually dependent and change with the heating rate (they reach a minimum for instantaneous heating). For a certain range of parameters, multiple (i.e. steady and oscillatory) states are possible. The oscillatory state has a form consisting of the steady mode with a simple harmonic sloshing motion superposed on it. A reduction in the heating rate permits heating of the liquid without triggering the oscillatory state. Transition between the steady and the oscillatory states involves a nonlinear instability process.

1. Introduction

The thermocapillary effect is recognized as an important factor is many areas of technology, where it could be either a dominant source of motion (e.g. zero-gravity containerless materials processing) or a contributing factor (e.g. conventional crystal growth or welding). Control and optimization of these processes critically depend on the complete understanding of all phenomena that may be induced by this effect. The focus of the present work is on studying these phenomena in the absence of any body forces, and especially in the absence of gravity.

The character of the response of a liquid adjacent to a non-isothermal interface depends on the orientation of the temperature gradient vector with respect to the interface. In the (geometrically) simplest case of a liquid layer with an initially flat interface resting on a plane uniformly heated solid plate, the temperature gradient is normal to the interface and it induces motion only when some critical conditions are met. This process, which is referred to as Marangoni instability, has been reviewed by Davis (1987). When the layer is non-uniformly heated, the temperature gradient vector has a component in the direction parallel to the interface and the thermocapillary effect always generates some motion, regardless of the magnitude of the temperature gradient. This configuration has been studied recently by Floryan & Chen (1994) who showed that an infinite continuous liquid layer may exist only when the external

temperature field (i.e. the external heating) satisfies restrictive existence conditions. The explicit form of these conditions was given in the case of negligible convective transport. Analysis of finite-length layers showed that if the external temperature field does not satisfy the existence conditions determined in the case of an infinite layer, large interfacial deformations occur, leading (possibly) to rupture of the layer if the cavity is made sufficiently long. One should note that the temperature fields satisfying the existence conditions are rather unusual and are unlikely to be encountered in practice. Also, the form of the existence conditions shows that it may not be possible to enforce them in the case of a general flow (i.e. one with convection effects present), and that the acceptable form of the external heating is a function of Reynolds number. The above discussion suggests that, in general, one should expect the response of the layer subject to steady non-uniform heating to consist of convection coupled with large interfacial distortions leading, possibly, to rupture of the layer.

The present study is focused on analysis of the dynamics of liquid layers subject to non-uniform steady heating. Our first goal is the determination of the pattern of interface deformation and the associated convection under conditions leading to large deformations, and the determination of the limits of existence of such layers with convective effects present. The answer to this leads us directly to our second objective, which is the determination of the behaviour of liquid layers under conditions when steady solutions do not exist. Since the governing equations are not amenable to analytical solutions under such conditions, we shall rely on numerical simulations. Development of a special algorithm that permits time-dependent simulation of thermocapillary convection with the interface undergoing large deformations therefore forms an integral part of this project. We shall demonstrate in this and the companion paper (Hamed & Floryan 2000) that different limiting factors affect the existence of the layers, depending on the type of external heating being applied. These factors include the interface approaching the bottom of the cavity (rupture of the layer; dry out at the bottom) and the interface becoming tangential to the sidewalls (dry out at the sidewalls). We shall also show that, depending on the type of external heating, the interface may begin to oscillate if this heating is applied too rapidly.

Our attention will be focused on two types of heating. The first one, described in this paper, corresponds to a cavity with differentially heated sidewalls which induce linear temperature variations along the interface. The companion paper (Hamed & Floryan 2000) describes the response of the layer subject to point heating as produced, for example, by laser heating. Neither types of heating satisfy the existence conditions for infinitely long layers.

The case of a cavity with differentially heated sidewalls has been widely studied and represents a convenient reference case. A complete understanding of this fairly simple flow configuration should provide a basis for analysis of complex configurations found in applications. Sen & Davis (1982) described the flow structure in an asymptotically long cavity in the Stokes limit and with an asymptotically small capillary numer $Ca = O(L^{-4})$, where L is the cavity length. Sen (1986) extended this analysis to $Ca = O(L^{-3})$ and showed the occurrence of large interfacial deformations. Floryan & Chen (1994) demonstrated that a continuous liquid layer subject to this type of heating cannot exist. The primary response of the layer consists of a large interfacial deformation leading, most likely, to rupture if the layer is sufficiently long. Laure, Roux & Ben Hadid (1990) and Ben Hadid & Roux (1992) described the differences in the flow patterns at the cold and hot ends of long cavities with non-deformable interface at higher values of Reynolds numbers. Zebib, Homsy & Meiburg (1985) and Carpenter & Homsy (1990) investigated the formation of boundary layers in a square

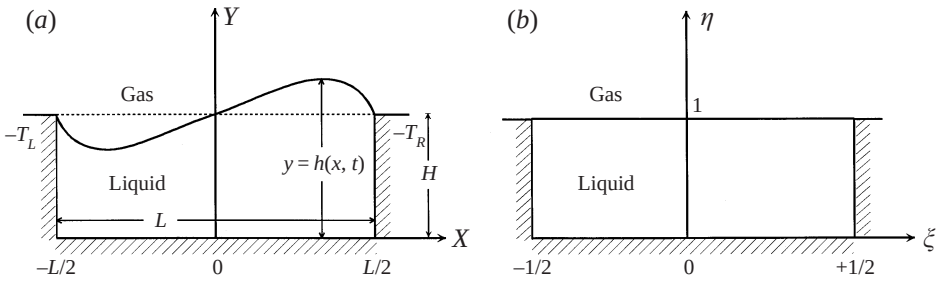

FIGURE 1. Sketch of the model problem. (*a*) Physical domain, (*b*) computational domain.

cavity with a fixed interface at high values of the Reynolds number. Peltier & Biringen (1993) used direct numerical simulation in studying the transition between steady and time-dependent convection in a cavity with a fixed interface. They concluded that an instability may occur in a cavity with a minimum aspect ratio of 2.3 and a minimum critical Marangoni number near 20 000; this instability depends upon coupling between large-scale thermal structures in the flow field and the temperature-sensitive interface. Chen & Hwu (1993) included effects of interface deformability and concluded, on the basis of simulations of convection in a rectangular cavity whose height was equal to half the length, that an instability may occur if the Marangoni number reaches critical value; this value was found to be around 2. Mundrane, Xu & Zebib (1995) and Mundrane & Zebib (1995) used an algorithm simplified through the use of a small interfacial deformation assumption and found only steady flows; their results contradict Chen & Hwu (1993). Liakopoulos & Brown (1993) investigated flow in a square cavity using complete model equations and found only steady flows, in agreement with Mundrane *et al.* (1995) and Mundrane & Zebib (1995). We shall discuss the above results and the reported disagreements in § 3.4.

The paper is organized as follows. § 2 gives the formulation and explains the notation used. § 3 gives a short description of the algorithm. § 4 provides a discussion of our results. § 5 gives a short summary of the main conclusions.

2. Problem formulation

Consider a liquid in a cavity of length L and height H, as shown in figure 1. The cavity, which is open from above, is formed by isothermal solid walls on the left and right sides, and by an insulated solid plate on the bottom. The liquid is incompressible, Newtonian, has density ρ, thermal conductivity k, specific heat per unit mass c, thermal diffusivity $\kappa = k/\rho c$, kinematic viscosity ν and dynamic viscosity μ. The free surface, described by $y = h(x, t)$, is bounded by a passive gas of negligible density and viscosity. This free surface is associated with a surface tension σ, which is a function of the local temperature. It is assumed, without loss of generality, that the pressure in the gas phase is negligible.

In the absence of gravity, the unsteady motion of the liquid is governed by the continuity, Navier–Stokes and energy equations subject to the following boundary conditions:

$$x = -L/2: \quad \boldsymbol{U} = 0, \qquad T = T_L, \tag{2.1a}$$

$$x = L/2: \quad \boldsymbol{U} = 0, \qquad T = T_R, \tag{2.1b}$$

$$y = 0: \quad \boldsymbol{U} = T_y = 0, \tag{2.1c}$$

$$F(x,y,t) = y - h(x,t) = 0: \quad F_t + \boldsymbol{U}\cdot\nabla F = 0, \tag{2.1d}$$

$$\boldsymbol{S}\cdot\boldsymbol{n} = 2\sigma\Lambda\boldsymbol{n} + \sigma_s\boldsymbol{t}, \tag{2.1e}$$

$$k\nabla T\cdot\boldsymbol{n} + h_g(T - T_g) = 0. \tag{2.1f}$$

In the above, $\boldsymbol{U} = u\boldsymbol{i} + v\boldsymbol{j}$ is the velocity vector, $\boldsymbol{i}$ and $\boldsymbol{j}$ are the unit vectors in the x- and y-directions, respectively, T is the temperature of the liquid, $\boldsymbol{S}$ is the stress tensor of the liquid, Λ stands for the mean curvature of the interface, ∇ denotes the nabla operator, $\boldsymbol{n}$ stands for the unit vector normal to the interface pointing outwards, $\boldsymbol{t}$ denotes the unit vector tangential to the interface, the subscripts x, y, t denote partial derivatives $\partial/\partial x$, $\partial/\partial y$, $\partial/\partial t$ respectively, and the subscripts n, s denote normal and tangential derivatives at the interface, respectively.

Equation (2.1d) is the kinematic condition at the liquid–gas interface. The stress balances at the interface are given by (2.1e). The jump in the normal stress across the interface is balanced by the surface tension times the mean curvature, and the jump in the shear stress at the interface is balanced by the surface tension gradient. The unit vectors are defined as follows:

$$\boldsymbol{n} = (-h_x\boldsymbol{i} + \boldsymbol{j})/N, \qquad \boldsymbol{t} = (\boldsymbol{i} + h_x\boldsymbol{j})/N, \tag{2.2}$$

where

$$N = (1 + h_x^2)^{1/2}. \tag{2.3}$$

The mean curvature Λ of the interface in (2.1e) has the definition

$$\Lambda = -\tfrac{1}{2}\nabla\cdot\boldsymbol{n} = \tfrac{1}{2}h_{xx}N^{-3}. \tag{2.4}$$

The thermal boundary condition at the interface is given by (2.1f) in which k is the thermal conductivity of the liquid, h_g is the heat transfer coefficient in the gas and $T_g(x,t)$ is the temperature in the gas phase. The thermal boundary condition presumes that $T_g(x,t)$ is known and that the heat transport at the liquid–gas interface can be described by using a heat-transfer coefficient h_g. The reader should note that $T_g(x,t)$, T_L and T_R may have to satisfy consistency conditions at the contact points.

Apart from boundary conditions (2.1), the liquid must also satisfy the mass conservation constraint. Since the liquid is assumed to be incompressible, its total volume must remain constant, i.e.

$$\int_{-L/2}^{L/2} h(x,t)\,\mathrm{d}x = V. \tag{2.5}$$

The problem is closed by specifying the type of contact made by the interface at the sidewalls. Here, we shall consider the fixed contact points case, i.e.

$$x = \pm\tfrac{1}{2}L: \qquad h(x,t) = H. \tag{2.6}$$

We shall use a linear equation of state for surface tension. In particular, we take

$$\sigma(T) = \sigma_* - \gamma(T - T_*), \tag{2.7}$$

where σ_* is the surface tension of the liquid at the reference temperature T_* and the constant γ is the negative of the derivative of the surface tension with respect to temperature.

We scale the problem by using L and H as the length scales for the x- and y-directions, respectively, u_* and u_*A as the velocity scales for u and v, respectively (where A is the cavity aspect ratio defined as H/L), $\mu u_*/(AH)$ as the pressure scale, H/u_* as

the time scale and σ_* as the surface tension scale. The dimensionless temperature T' is defined as

$$T - T_* = (T_{max} - T_{min})T', \qquad T_g - T_* = (T_{max} - T_{min})T'_g. \tag{2.8}$$

Here T_{max} and T_{min} denote the maximum and the minimum of the interface temperature, respectively. The characteristic velocity u_* is derived from the so-called Marangoni effect, i.e. the jump in the shear along the interface balances the surface tension gradient. This leads to

$$u_* = \gamma(T_{max} - T_{min})/\mu. \tag{2.9}$$

With the above definitions the dimensionless equations (with the primes dropped) can be written in the form

$$u_x + v_y = 0, \tag{2.10a}$$

$$Re[u_t + A(uu_x + vu_y)] = -p_x + A^2 u_{xx} + u_{yy}, \tag{2.10b}$$

$$ReA^2[v_t + A(uv_x + vv_y)] = -p_y + A^2(A^2 v_{xx} + v_{yy}), \tag{2.10c}$$

$$Ma[T_t + A(uT_x + vT_y)] = A^2 T_{xx} + T_{yy}, \tag{2.10d}$$

where p denotes pressure.

Reynolds number Re and Marangoni number Ma have the standard definitions, i.e.

$$Re = \frac{u_* H}{\nu} = \frac{\gamma(T_{max} - T_{min})H}{\mu\nu}, \qquad Ma = \frac{u_* H}{\kappa} = \frac{\gamma(T_{max} - T_{min})H}{\mu\kappa}. \tag{2.11}$$

The boundary conditions (2.1) transform to

$$x = -\tfrac{1}{2}: \quad u = v = 0, \qquad T = T_L, \tag{2.12a}$$

$$x = \tfrac{1}{2}: \quad u = v = 0, \qquad T = T_R, \tag{2.12b}$$

$$y = 0: \quad u = v = T_y = 0, \tag{2.12c}$$

$$y = h(x,t): \quad h_t + A(uh_x - v) = 0, \tag{2.12d}$$

$$-p + \frac{2A^2[v_y - h_x u_y + A^2 h_x(-v_x + h_x u_x)]}{(1 + A^2 h_x^2)} = \frac{A^3 Ca^{-1}(1 - A^{-1}CaT)h_{xx}}{(1 + A^2 h_x^2)^{3/2}}, \tag{2.12e}$$

$$2A^2 h_x(-u_x + v_y) + (1 - A^2 h_x^2)(A^2 v_x + u_y) = -(T_x + h_x T_y)(1 + A^2 h_x^2)^{1/2}, \tag{2.12f}$$

$$(-A^2 h_x T_x + T_y)(1 + A^2 h_x^2)^{-1/2} + Bi[T - T_g(x,t)] = 0, \tag{2.12g}$$

where (2.12*d*) is the kinematic condition, (2.12*e*) and (2.12*f*) are the stress balances in the normal and tangential directions, respectively, and (2.12*g*) describes the heat transfer condition. In (2.12*e*) Ca is the capillary number, given by

$$Ca = \frac{\mu u_*}{\sigma_*} = \frac{\gamma(T_{max} - T_{min})}{\sigma_*}. \tag{2.13}$$

The Biot number Bi in (2.12*g*) is defined by

$$Bi = \frac{h_g H}{k} \tag{2.14}$$

and measures the heat transport between the gas and the liquid phases. The dimensionless form of the mass constraint retains the same form as (2.5). The contact

conditions assume the form

$$x = \pm\tfrac{1}{2}: \qquad h(x,t) = 1. \tag{2.15}$$

Steady flow of the liquid is described by the same field equations with time derivatives omitted, and by the same boundary conditions with the kinematic condition (2.12*d*) simplified through elimination of h_t.

3. Numerical method

This study is concerned with the steady and unsteady motions of the liquid. The steady form of the equations is solved using the algorithm developed by Chen & Floryan (1994). The following description is focused on the unsteady algorithm and is limited to a short outline only. Details of the algorithm, including accuracy and stability testing, are given by Hamed & Floryan (1998).

Flow problem (2.10), (2.12), and (2.15) with constraint (2.5) has to be solved numerically on an irregular, time-dependent solution domain whose shape is determined by the location of the free surface $h(x,t)$. Application of the transformation

$$\xi = x, \qquad \eta = \frac{y}{h(x,t)} \tag{3.1}$$

maps this domain onto a fixed rectangular domain in the computational (ξ,η) plane (see figure 1) permitting use of the standard finite-difference discretization techniques for spatial derivatives. The explicit form of the mapping function $h(x,t)$ is not known and has to be determined as a part of the numerical procedure.

The field variables are expressed in terms of the streamfunction–vorticity formulation in order to guarantee enforcement of the incompressibility condition. Field equations (2.10) take the following form:

$$\nabla^2\psi + \omega = 0, \tag{3.2a}$$

$$\omega_t - \eta h^{-1} h_t \omega_\eta + \frac{A}{h}(\psi_\eta \omega_\xi - \psi_\xi \omega_\eta) = \nabla^2\omega/Re, \tag{3.2b}$$

$$T_t - \eta h^{-1} h_t T_\eta + \frac{A}{h}(\psi_\eta T_\xi - \psi_\xi T_\eta) = \nabla^2 T/Ma, \tag{3.2c}$$

where

$$u = \psi_y, \quad v = \psi_x, \quad \omega = v_x - u_y, \tag{3.2d}$$

$$\nabla^2 = A^2\frac{\partial^2}{\partial\xi^2} - 2A^2\eta h_\xi h^{-1}\frac{\partial^2}{\partial\xi\partial\eta} + h^{-2}(A^2\eta^2 h_\xi^2 + 1)\frac{\partial^2}{\partial\eta^2} + (2h_\xi^2 - hh_{\xi\xi})\eta A^2 h^{-2}\frac{\partial}{\partial\eta}.$$

The boundary conditions take the form

$$\xi = -\tfrac{1}{2}: \quad \psi = \psi_\xi = 0, \qquad T = T_L, \tag{3.2e}$$

$$\xi = \tfrac{1}{2}: \quad \psi = \psi_\xi = 0, \qquad T = T_R, \tag{3.2f}$$

$$\eta = 0: \quad \psi = \psi_\eta = 0, \qquad T_\eta = 0, \tag{3.2g}$$

$$\eta = 1: \quad h_t + A\psi_\xi = 0, \tag{3.2h}$$

$$-p + 2\frac{(A^4 h_\xi \psi_{\xi\xi\xi} - (1+h_\xi^2)A^2 h^{-1}\psi_{\xi\eta} + A^2 h_\xi h^{-2}(1 + A^2 h_\xi^2 - A^2 h h_{\xi\xi})\psi_\eta)}{(1 + A^2 h_\xi^2)}$$
$$= Ca^{-1}(A - CaT)A^2 h_{\xi\xi}(1 + A^2 h_\xi)^{3/2}, \tag{3.2i}$$

$$-A^2(1-A^2h_\xi^2)\psi_{\xi\xi}+h^{-2}(1+A^2h_\xi^2)^2\psi_{\eta\eta}-2A^2h_\xi h^{-1}(1+A^2h_\xi^2)\psi_{\xi\eta}$$
$$+\left[A^2(1-A^2h_\xi^2)hh_{\xi\xi}+2A^2h_\xi^2(1+A^2h_\xi^2)\right]h^{-2}\psi_\eta=-T_\xi(1+A^2h_\xi^2)^{1/2}, \quad (3.2j)$$

$$(1+A^2h_x^2)^{1/2}h^{-1}T_\eta-A^2h_\xi(1+A^2h_\xi^2)^{-1/2}T_\xi+Bi(T-T_g(\xi,t))=0. \quad (3.2k)$$

One- and two-step implicit methods with accuracy $O(\Delta t)$ and $O(\Delta t^2)$ have been used for temporal discretization, where Δt denotes the time step. Typically, calculations were carried out over the first few time steps using the (self-starting) one-step method and then continued using the more accurate (but not self-starting) two-step method. Certain cases were repeated using only the one-step method with a much smaller step size in order to check the accuracy and consistency of the calculations. Both methods use the same second-order-accurate spatial discretization and have been found to be stable. The following outline is focused on the two-step method.

It is assumed that all flow quantities at times $t=(n-1)\Delta t$ and $t=n\Delta t$ are available. Temperature $T_g(\xi,t)$ in the gas phase is changed to its value at $t=(n+1)\Delta t$ and the flow and the temperature fields together with the location of the interface at time $t=(n+1)\Delta t$ are sought. The field equations are solved using a Picard-type iteration on the shape of the interface and on the value of the streamfunction at the interface. Initial estimates of the location of the interface and the value of the streamfunction there are made and the flow problem is solved without enforcing the normal stress and kinematic conditions at the interface. This is referred to as the inner problem or the inner solution. Once the inner problem has been solved, the normal stress condition is used to determine the new location of the interface, and the kinematic condition is used to evaluate the new value of the streamfunction at the interface. We shall refer to this part of the solution process as the outer problem or the outer solution. The complete solution procedure involves iterations between the inner and the outer problems until all conditions are satisfied with the desired accuracy. We shall refer to the above iteration as the outer iteration.

3.1. *Inner problem*

The field equations are written at time $t=(n+1)\Delta t$ in the form

$$\nabla^2\psi^{n+1}+\omega^{n+1}=0, \quad (3.3a)$$

$$\frac{3\omega^{n+1}-4\omega^n+\omega^{n-1}}{2\Delta t}+\frac{A}{h^{n+1}}(\psi_\eta^{n+1}\omega_\xi^{n+1}-\psi_\xi^{n+1}\omega_\eta^{n+1})$$
$$+\frac{\eta A(\psi_\xi)_b^{n+1}\omega_\eta^{n+1}}{h^{n+1}}-\frac{\nabla^2\omega^{n+1}}{Re}=0, \quad (3.3b)$$

where ω^{n+1} has been replaced by backward, second-order finite-difference approximation, h_t^{n+1} was replaced by $(\psi_\xi^{n+1})_b$ using (3.2*h*), superscripts $n-1$, n, $n+1$ refer to time steps, b denotes the value of the filed variable at the interface and h^{n+1} is considered known. The energy equation has the same form as (3.3*b*) with ω replaced by T, and Re replaced Ma.

A rectangular computational grid of size $\Delta\xi$, $\Delta\eta$ in the (ξ,η)-directions is considered, with grid lines parallel to the ξ- and η-axes and such that the grid fits exactly the geometry of the computational domain, with the side and bottom walls and the interface as certain grid lines. Around a typical interior grid point (ξ_0,η_0) we adopt the convention that quantities at (ξ_0,η_0) and eight neighbouring points are denoted by

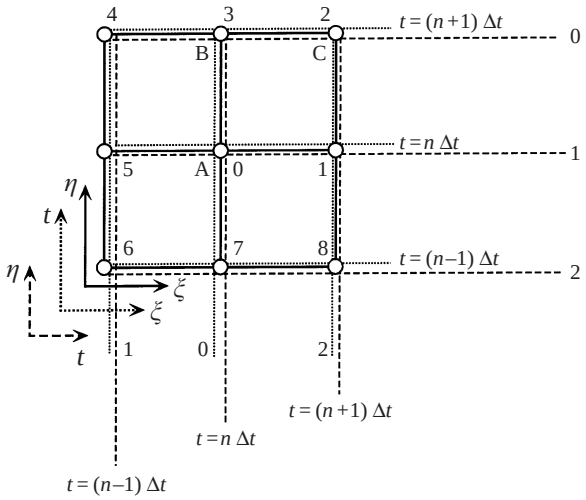

FIGURE 2. Sketch of typical computational molecules. Solid lines describe spatial discretization while dotted and dashed lines describe temporal discretization in the (ξ, t)- and (η, t)-planes, respectively.

subscripts $0, 1, \ldots, 8$ as shown in figure 2. Equations (3.3) are written at each interior grid point (point A in figure 2) and the spatial derivatives are approximated by using second-order finite differences in the usual manner, to give

$$-2(A_1 + A_2)\psi_0^{n+1} + A_1\psi_1^{n+1} - A_3\psi_2^{n+1} + (A_2 + A_4)\psi_3^{n+1} + A_3\psi_4^{n+1} + A_1\psi_5^{n+1} - A_3\psi_6^{n+1} + (A_2 - A_4)\psi_7^{n+1} + A_3\psi_8^{n+1} + \omega_0^{n+1} = 0, \tag{3.4a}$$

$$\begin{aligned} -[2(A_1 + A_2) + ReA_6]\omega_0^{n+1} &+ [A_1 - ReA_5(\psi_3^{n+1} - \psi_7^{n+1}]\omega_1^{n+1} - A_3\omega_2^{n+1} \\ &+ [A_2 + A_4 - ReA_7 + ReA_5(\psi_1^{n+1} - \psi_5^{n+1})]\omega_3^{n+1} + A_3\omega_4^{n+1} \\ &+ [A_1 + ReA_5(\psi_3^{n+1} - \psi_7^{n+1})]\omega_5^{n+1} - A_3\omega_6^{n+1} \\ &+ [A_2 - A_4 + ReA_7 - ReA_5(\psi_1^{n+1} - \psi_5^{n+1})]\omega_7^{n+1} \\ &+ A_3\omega_8^{n+1} + ReA_6\omega_0^n = 0, \end{aligned} \tag{3.4b}$$

where

$$A_1 = \frac{A^2}{(\Delta\xi)^2}, \quad A_2 = [1 + \eta^2 A^2 (h_\xi^{n+1})^2](h^{n+1}\Delta\eta)^{-2}, \quad A_3 = \eta A^2 h_\xi^{n+1}(2h^{n+1}\Delta\xi\Delta\eta)^{-1},$$

$$A_4 = \eta A^2[2(h_\xi^{n+1})^2 - h^{n+1}h_{\xi\xi}^{n+1}][2(h^{n+1})^2\Delta\eta]^{-1}, \quad A_5 = \frac{A}{(4h^{n+1}\Delta\xi\Delta\eta)}, \quad A_6 = (\Delta t)^{-1},$$

$$A_7 = \eta(\psi_\xi^{n+1})_b(2h^{n+1}\Delta\eta)^{-1}.$$

The boundary conditions for (3.4) are given by (3.2*e–g*, *j*). For (3.4*a*), the values of ψ^{n+1} are known at all grid points on the solid walls, and are known from the previous outer iteration (or from the previous time step in the case of the first outer iteration) at the interface. For (3.4*b*), a boundary condition for ω^{n+1} is required at the grid points on the sidewalls. Here, we use the second-order approximation for the sidewalls

$$\omega_w^{n+1} = A^2(\psi_{i+1}^{n+1} - 8\psi_i^{n+1})/(2\Delta\xi^2), \tag{3.5a}$$

where subscript w refers to the wall values, subscript i refers to the internal grid point closest to w and subscript $(i+1)$ refers to the next grid point in the same direction. A similar formula for the bottom of the cavity has the form

$$\omega_w^{n+1} = (\psi_{i+1}^{n+1} - 8\psi_i^{n+1})/[2\Delta\eta^2(h^{n+1})^2]. \tag{3.5b}$$

In the above, h^{n+1} is considered to be known from the previous outer iteration (or from the previous time step in the case of the first outer iteration). The boundary condition at the interface is obtained by substituting (3.2*j*) into (3.2*a*), resulting in

$$\omega_b^{n+1} = -2A^2(1 + A^2(h_\xi^{n+1})^2)^{-1}(\psi_{\xi\xi}^{n+1})_b + (h^{n+1})^{-1}(1 + A^2(h_\xi^{n+1})^2)^{-1}$$
$$\times\{h^{n+1}(1 + A^2(h_\xi^{n+1})^2)^{1/2}(T_\xi^{n+1})_b + 2A^2h_{\xi\xi}^{n+1}(\psi_\eta^{n+1})_b\}. \tag{3.6}$$

In the above $(\psi_{\xi\xi}^{n+1})_b$, h^{n+1}, h_ξ^{n+1}, $h_{\xi\xi}^{n+1}$ are considered to be known; h_ξ^{n+1} and $h_{\xi\xi}^{n+1}$ are evaluated using standard central-difference approximations based on the values of h^{n+1} from the previous outer iteration (or from the previous time step in the case of the first iteration). Evaluation of $(\psi_{\xi\xi}^{n+1})_b$ is discussed in § 3.2. The temperature gradient $(T_\xi^{n+1})_b$ is evaluated using the standard central-difference approximation and $(\psi_\eta^{n+1})_b$ is determined using the one-sided difference approximation. All spatial discretization formulas are second-order accurate.

For the energy equation, values of T^{n+1} are known at the sidewalls. At the remaining two boundaries, T^{n+1} is determined from the discretized boundary conditions (3.2*g*) and (3.2*k*) using the second-order finite-difference formulas.

Assuming that the location of the interface h^{n+1} and the value of the streamfunction ψ_b^{n+1} at the interface are known, the problem (3.4) supplemented by the energy equation and the boundary conditions described above can be solved either directly or iteratively. Typically, in the present study, we used the Gauss–Seidel iteration procedure. We shall refer to this process as the inner iteration. Linear extrapolation based on the values of flow quantities at $t = (n-1)\Delta t$ and $t = n\Delta t$ was used to provide the initial guess at time $t = (n+1)\Delta t$. The systematic iterative procedure between the various equations consisted of performing one complete Gauss–Seidel iteration of (3.4*a*), followed by a similar iteration of (3.4*b*) and then a complete iteration of the energy equation, followed by a recalculation of the boundary values of ω^{n+1} and T^{n+1}. The iteration were performed until the convergence criteria, $|q_{i+1} - q_i| < \varepsilon_1$ and $|\mathrm{Res}_i| < \varepsilon_1$ with $\varepsilon_1 = 10^{-6}$–10^{-8} were satisfied at all grid points. In the above, q stands for any of the flow quantities (ψ, ω, T), Res denotes residuum of any of the discretized field equations, and subscript i denotes the (inner) iteration number.

3.2. *Outer problem*

The outer problem consists of evaluation of the new location of the interface and the new value of ψ_b^{n+1} that correspond to the most recent solution of the inner problem. The interface is determined from the normal stress condition (3.2*i*) subject to the contact conditions (2.15) and the volume constraint (2.5). The field variables determined by the inner problem are kept constant during solution of the outer problem.

The normal stress condition (3.2*i*) involves the pressure at the interface which has to be evaluated on the basis of the known solution of the inner problem. Equations (2.10*b*, *c*) are solved for the components of the pressure gradient, transferred into the (ξ, η)-plane using (3.1), expressed in a form suitable for the interface (i.e. for $\eta = 1$)

and combined to yield

$$p_\xi = A^2 h_\xi \omega_\xi - (1 + A^2 h_\xi^2) h^{-1} \omega_\eta$$
$$-\frac{ReA}{h^2}\psi_\eta((1 + A^2 h_\xi^2)\psi_{\xi\eta} + h_\xi h^{-1}(A^2 h_{\xi\xi} h - A^2 h_\xi^2 - 1)\psi_\eta)$$
$$-Re[(1 + A^2 h_\xi^2) h^{-1}\psi_{\eta t} - A^2 h_\xi \psi_{\xi t} + A h^{-2}\psi_\eta[(1 + A^2 h_\xi^2)\psi_\xi - 2A^2 h h_\xi \psi_{\xi\xi}]]. \quad (3.7a)$$

Equation (3.7*a*) is integrated from $\xi = 0$ to $\xi = a$ to get

$$\tilde{p}(a) = A^2[(h_\xi \omega)_{\xi=a} - (h_\xi \omega)_{\xi=0}] - A^2 \int_0^a h_{\xi\xi}\omega \, \mathrm{d}\xi + \int_0^a B \, \mathrm{d}\xi, \quad (3.7b)$$

where the first three terms on the right-hand side resulted from the integration by parts of the first term on the right-hand side of (3.7*a*) and B stands for the remaining terms on the right-hand side of (3.7*a*). Integrals in (3.7*b*) are evaluated using the trapezoidal rule based on the same grid as used in the determination of the flow field. Direct numerical integration of (3.7*a*) is not advisable because it requires knowledge of the (undefined) values of vorticity at the contact points.

An expression for the pressure can be written in general as

$$p(\xi, 1, t) = \tilde{p}(\xi, 1, t) + K(t), \quad (3.8)$$

where $\tilde{p}$ denotes the normalized pressure satisfying condition $\tilde{p}(0, 1, t) = 0$ and $K(t)$ denotes an unknown additive constant.

The spatial derivatives with respect to η in (3.7*a*) are evaluated using one-sided second-order finite-difference approximations based on the grid used in the inner problem. The mixed derivative of ψ at $t = (n+1)\Delta t$ with respect to spatial coordinates $\psi_{\xi\eta}$ is evaluated at the interface (point B in figure 2) according to the formula

$$(\psi_{\xi\eta})_3 = [3(\psi_2 - \psi_4) - 4(\psi_1 - \psi_5) + \psi_8 - \psi_6]/(4\Delta\xi\Delta\eta) + O(\Delta\xi^2) + O(\Delta\eta^2). \quad (3.9)$$

The mixed derivatives $\psi_{\xi t}$ and $\psi_{\eta t}$ are evaluated using the formulae

$$(\psi_{\xi t})_B = [3(\psi_2^{n+1} - \psi_1^{n+1}) - 4(\psi_2^n - \psi_1^n) + \psi_2^{n-1} - \psi_1^{n-1}]/(4\Delta t\Delta\xi) + O(\Delta t^2) + O(\Delta\xi^2), \quad (3.10)$$

$$(\psi_{\eta t})_C = [3(3\psi_0^{n+1} - 4\psi_1^{n+1} + \psi_2^{n+1}) - 4(3\psi_0^n - 4\psi_1^n + \psi_2^n)$$
$$+3\psi_0^{n-1} - 4\psi_1^{n-1} + \psi_2^{n-1}]/(4\Delta t\Delta\eta)$$
$$+O(\Delta t)^2 + O[(\Delta t)^2(\Delta\eta)^2] + O(\Delta\eta)^2, \quad (3.11)$$

where the subscripts refer to the points shown in figure 2.

The normal stress condition (3.2*i*) can be interpreted as a nonlinear ordinary differential equation for $h(\xi)$ with the known variable coefficients expressed in terms of ψ^{n+1}, T^{n+1}, P^{n+1}. This equation involves an unknown pressure normalization constant K and is subject to boundary conditions (2.15) and constraint (2.5). It is assumed that a sufficiently good approximation of the solution is available, i.e.

$$h = h_o + h_1, \qquad K = K_o + K_1, \quad (3.12)$$

where h_o, K_o are known and $h_1 \ll 1$, $K_1 \ll 1$. Newton–Raphson linearization leads

to the following problem for h_1, K_1:

$$h_{1\xi\xi} + H(\xi)h_{1\xi} = M(\xi) + K_1 N(\xi), \tag{3.13a}$$

$$h_1(-\tfrac{1}{2}) = 0, \tag{3.13b}$$

$$h_1(\tfrac{1}{2}) = 0, \tag{3.13c}$$

$$\int_{-1/2}^{1/2} h_1 \,\mathrm{d}\xi = 0, \tag{3.13d}$$

where

$$H(\xi) = -3A^2 h_{o\xi} h_{o\xi\xi}(1 + A^2 h_{o\xi}^2)^{-1} - Ca(A - CaT)^{-1}(1 + A^2 h_{o\xi}^2)^{-1/2} \times [4A^2 \psi_{\xi\xi} - 4A^2 h_{o\xi\xi} h_o^{-1} \psi_\eta + 2(1 + A^2 h_{o\xi}^2)\omega],$$

$$M(\xi) = -Ca(A - CaT)^{-1}(1 + A^2 h_{o\xi}^2)^{1/2}[2(1 + A^2 h_{o\xi}^2) h_o^{-1} \psi_{\xi\eta} - 2A^2 h_{o\xi} \psi_{\xi\xi} - 2(1 + A^2 h_{o\xi}^2 - A^2 h_{o\xi\xi} h_o) h_o^{-2} h_{o\xi} \psi_\eta + (1 + A^2 h_{o\xi}^2)(\tilde{p} + K_o)] - h_{o\xi\xi},$$

$$N(\xi) = -\frac{Ca(1 + h_{o\xi}^2)^{3/2}}{(A - CaT)A^2}.$$

The form of conditions (3.13*b–d*) assumes that h_o satisfies the contact conditions (2.15) and the volume constraint (2.5). In the calculations, h_o is taken to be the shape of the interface from the previous outer iteration. For a sufficiently small time step a good approximation h_o of the interface is always available and this permits taking full advantage of the quadratic rate of convergence of the iterative process based on linearization (3.13). Typically, one or two iterations would reduce the error to several orders of magnitude less than the error accepted in the solution of the inner problem.

During each of the above iterations one has to solve problem (3.13). This is a linear problem, thus its solution consists of a superposition of two linearly independent solutions and a particular solution of the inhomogeneous problem. Two boundary conditions (3.13*b*, *c*) and volumetric constraint (3.13*d*) provide the required three conditions for the determination of the two constants of superposition and the pressure constant K_1.

Problem (3.13) is solved directly. Equation (3.13*a*) is discretized using the standard central-difference formulas and (3.13*d*) is approximated using the trapezoidal rule. The grid already used for the determination of the flow field is used in both cases. The structure of the resulting matrix, together with the optimized matrix inversion algorithm, are described by Chen & Floryan (1994).

Kinematic condition (3.2*h*) is written for time $t = (n+1)\Delta t$ and the time derivative h_t^{n+1} is replaced by a backward, second-order, finite-difference approximation, i.e.

$$(\psi_\xi^{n+1})_b = -\frac{1}{A}(3h^{n+1} - 4h^n + h^{n-1})/(2\Delta t) + O(\Delta t)^2, \tag{3.14}$$

where h^{n-1}, h^n denote the known locations of the interface at times $t = (n-1)\Delta t$, $t = n\Delta t$, respectively, and h^{n+1} denotes the most recent approximations of h at time $t = (n+1)\Delta t$. Integration of (3.14) gives

$$(\psi^{n+1})_b = \frac{1}{A}\left(3\int_{-1/2}^{\xi} h^{n+1}\,\mathrm{d}\xi - 4\int_{-1/2}^{\xi} h^n \,\mathrm{d}\xi + \int_{-1/2}^{\xi} h^{n-1}\,\mathrm{d}\xi\right) \Big/ (2\Delta t), \tag{3.15}$$

where all integrals are evaluated using the trapezoidal rule. Solution of the inner problem requires knowledge of ψ_b^{n+1}, $(\psi_\xi^{n+1})_b$, $(\psi_{\xi\xi}^{n+1})_b$. ψ_b^{n+1} is given by (3.15), $(\psi_{\xi\xi}^{n+1})_b$ is given by (3.14), $(\psi_{\xi\xi\xi}^{n+1})_b$ is evaluated using the derivative of the kinematic condition $(\psi_{\xi\xi}^{n+1})_b = -h_{\xi t}^{n+1}$ where $h_{\xi t}^{n+1}$ is evaluated using a finite-difference approximation similar to (3.10).

3.3. *Outer iterations*

A complete iterative cycle consists of determination of the flow field (inner problem) followed by determination of the new approximation for h^{n+1} and ψ_b^{n+1} (outer problem). Such (outer) iterations are carried out until convergence criteria $|h_{i+1}^{n+1} - h_i^{n+1}| < \varepsilon_2$ and $|\mathrm{Res}_i| < \varepsilon_2$ are satisfied at all grid points along the interface. In the above, subscripts i, $i+1$ denote the (outer) iterations and Res stands for the residuum of the normal stress condition. Calculations were typically carried out with $\varepsilon_2 = 10^{-6}$–10^{-8}.

3.4. *Verification of the algorithm*

Details of the accuracy, grid convergence and stability testing can be found in Hamed & Floryan (1998). Various tests confirmed that the algorithm is stable and delivers the theoretically predicted accuracy. All numerical results presented in the next section are at least two-digits accurate. Both spatial and temporal grid resolutions have been selected using grid convergence studies carried out in the manner described by Hamed & Floryan (1998). A grid with $\Delta\eta = \Delta x = 0.05$ and $\Delta t = 0.2$ provides sufficient accuracy for most cases considered. Certain cases were spot checked by repeating calculations either with a smaller grid size or with a different method of temporal discretization.

A part of the algorithm verification process involved repetition of the results reported in the literature. It was also of interest to resolve the contradiction, already referred to in the Introduction, in the results reported by Chen & Hwu (1993) and Mundrane *et al.* (1995) and Mundrane & Zebib (1995), and the agreement between the last group and Liakopoulos & Brown (1993). We repeated one test case reported by the first two groups ($A = 0.5$, $Re = 220$, $Ma = 2.2$, $Ca = 0.01$, $Bi = 0$) and found the transition to oscillatory convection exactly as reported by Chen & Hwu (1993). The reader may note that Chen & Hwu (1993) solve the complete problem while Mundrane *et al.* (1995) and Mundrane & Zebib (1995) use simplified methods based on linearized interfacial boundary conditions; such linearizations partially decouple the interface from the flow field. We have programmed a method based on expansions in Ca, with $Ca \to 0$, and concluded, by comparing results produced by this method and by the complete algorithm, that such simplified methods are unable to reproduce the time-dependent phenomena. When the problem is such that the transient effects eventually die out, the simplified algorithm produces the correct steady limit. The simplified algorithm is equivalent to the steady algorithm for the small deformation problems described in detail by Chen & Floryan (1994), with the iterative solution process interpreted as a certain 'non-physical' flow transient.

The case considered by Liakopoulos & Brown (1993) involves a short cavity ($A = 1$) where the convection may have only a steady form, as discussed in the next section. The simplified algorithm correctly predicts this flow. This is underscored by the fact that we have reproduced results of Liakopoulos & Brown (1993) using the complete algorithm and in all cases obtained steady flows.

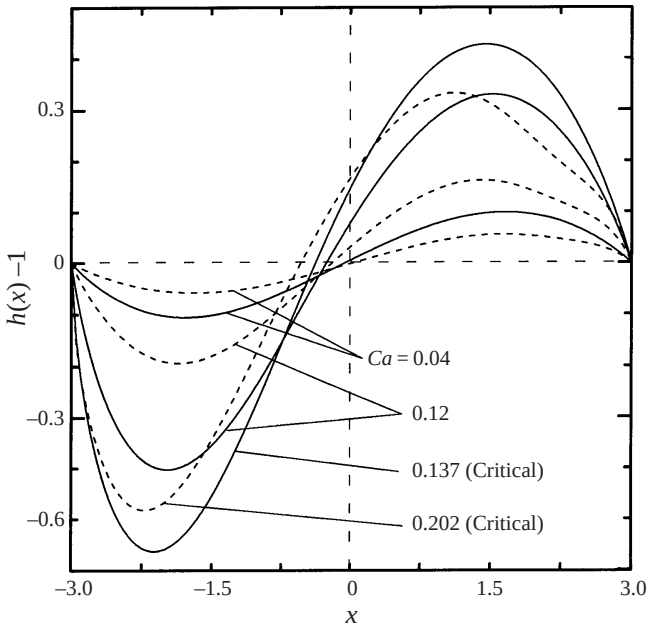

FIGURE 3. Shape of the interface as a function of capillary number Ca for $L = 6$. Solid and dashed lines correspond to $Re = 1$ and $Re = 400$, respectively.

4. Discussion of results

We shall investigate the behaviour of the liquid contained in the cavity shown in figure 1. The volume of the liquid is such that the interface is initially (i.e. before the application of any heating) flat. The cavity sidewalls are differentially heated. The temperature distribution in the gas phase along the interface has a linear form, i.e.

$$T_g(x) = -x. \tag{4.1}$$

The sidewalls have temperatures $T_L = \frac{1}{2}$ and $T_R = -\frac{1}{2}$ and this implies that the temperature gradient along the interface is a function of the cavity length L. Since this heating does not satisfy the interface existence conditions (see § 1 for a discussion), it is expected that the interface will undergo large deformations leading, possibly, to rupture of the layer. The main objective of our work is the determination of the form of the interface deformation and the limits of existence of a continuous layer. In order to simplify the following discussion, we shall only consider the case $Ma = 0$ ($Pr = 0$), $Bi = \infty$. The first condition limits our results to highly conductive liquids, such as liquid metals, where conductive heat transport dominates over convective heat transport. The second condition implies a very high heat transfer coefficient in the gas phase at the interface which makes the temperature of the interface effectively equal to the temperature of the gas phase.

As a first step, we shall discuss the steady response of the liquid to the external heating described above.

4.1. *Steady-state response*

Figure 3 illustrates the evolution of the interface deformation pattern as a function of the capillary number Ca for Reynolds numbers $Re = 1$, $Re = 400$ and the cavity length $L = 6$. The reader may recall that increasing Ca corresponds to the interface

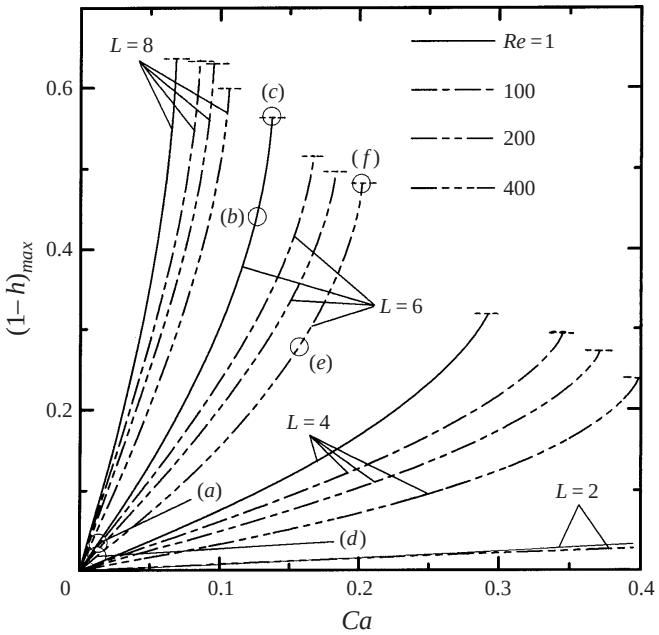

FIGURE 4. The maximum of the interface deformation on the left side of the cavity as a function of capillary number Ca. The flow and deformation patterns corresponding to points (a), (b), (c) are shown in figure 5, and those corresponding to points (d), (e), (f) are shown in figure 6.

becoming progressively softer. The interface bulges in at the hot end and bulges out at the cold end. The maximum deformation occurs for small Ca in the area where the interface bulges out; for larger Ca the maximum occurs in the area where the interface bulges in. An increase of Ca results in a more rapid increase of the deformation at the hot end. Results shown in figure 3 demonstrate that the interface there evolves toward becoming tangential to the hot wall at the contact point. This implies formation of a dryout at the sidewall. Another alternative is that the assumed location of the contact point cannot be maintained and the contact line will move downwards. Since the model described in § 2 breaks down under such circumstances, we have decided to limit our investigation to conditions that lead to a contact angle between the interface and the hot wall of no less than 5°. Figure 4 presents the evolution of the maximum of the interface deformation, in the area where the interface bulges in, as a function of the capillary number Ca for the cavity lengths $L = 2$, 4, 6, 8 and for the Reynolds numbers $Re = 1$, 100, 200, 400, respectively. The deformation curves shown in this figure are terminated when the tangency condition is violated. The form of these curves shows that when Ca increases and the interface approaches a position tangent to the sidewall (at the left contact point), the amplitude of the deformation increases at a rapidly accelerating rate. It is clear that when Ca reaches a certain critical value Ca_{cr} a continuous interface connecting contact points cannot exist. This value of $Ca = Ca_{cr}$ defines a limit point for the system. It is likely that for $Ca > Ca_{cr}$ the liquid may separate into a drop attached to the left wall and the rest of it filling the bottom of the cavity, with the left contact point located significantly below its original position. The reader should note that we were unable to determine the true value of Ca_{cr} and used in our discussion the value of Ca corresponding to the contact angle of 5° instead.

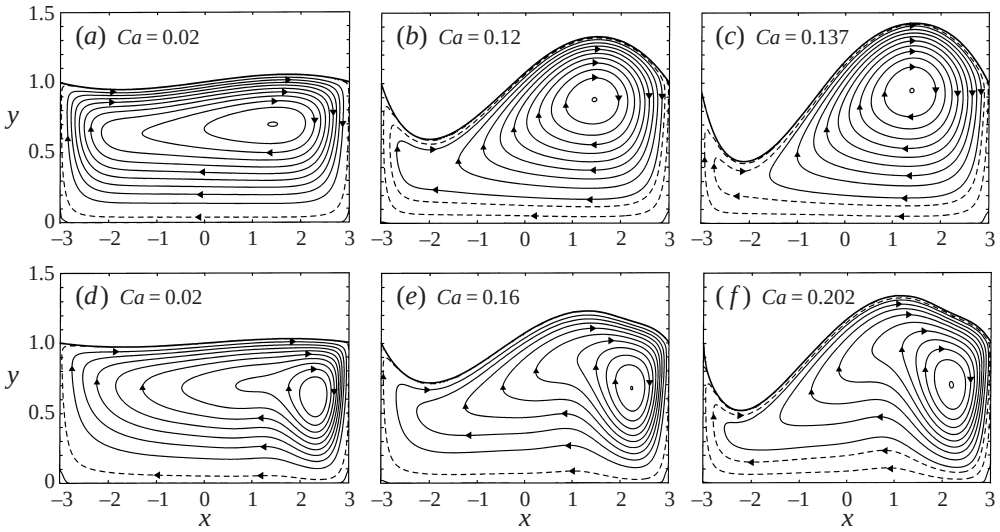

FIGURE 5. The evolution of the flow and deformation patterns as a function of capillary number Ca for $L = 6$ and (*a–c*) $Re = 1$, (*d–f*) $Re = 400$: (*a–f*) respectively correspond to points (*a–f*) in figure 4. Contour lines are shown every 10% of ψ_{max} (solid lines); the dashed lines show 1% of ψ_{max} in (a, d, e) and 1% and 5% of ψ_{max} in (b, c, f). In (*a–f*) $|\psi_{max}| = 0.2470$, 0.4430, 0.5294, 0.2604, 0.3104, 0.3319 respectively.

Figure 5 displays the flow and deformation patterns as a functions of Ca for $Re = 1$ and $Re = 400$ for cavity length $L = 6$. Comparison of figure 5(*a–c*) with 5(*d–f*) shows that the centre of the recirculating vortex moves closer to the cold wall when Re increases. The end circulations at the hot and cold walls are totally different. This is in qualitative agreement with Laure *et al.* (1990) and Ben Hadid & Roux (1992), who analysed these differences in detail in the case of a non-deformable interface. They demonstrated that these differences result from the increase of Re. Our results show that these differences are due to the deformation as well as to the Reynolds number effects; they can be seen even for $Re = 1$ (see figure 5*a–c*). An increase of Re also results in the formation of a strong vortex core. This core becomes approximately inviscid (with a constant vorticity in its interior) and its structure corresponds well to Batchelor's (1956) model for steady laminar flow with closed streamlines at large Re. The minimum pressure associated with the vortex causes a small depression in the surface elevation above the vortex (see figures 3 and 5(*d–f*)).

Figures 6(*a*) and 6(*b*) illustrate the evolution of the interface deformation as a function of Re for cavity lengths $L = 2$, 4, 6, 8, respectively. It can be seen that for $L = 2$ the magnitude of the deformation increases somewhat when the Reynolds number increases to $Re = 50$ (regardless of the value of Ca) and it remains essentially unchanged for $Re > 50$ (see figure 6*a*). This magnitude remains small in absolute terms. Doubling of the length to $L = 4$ increases the deformation by almost a factor of 10 (see figure 6*a*). Increase of Re from 0 to 500 smoothly reduces the deformation by a factor of 2. Further increase of cavity length to $L = 6$ increases the deformation by another factor of 3–4 compared to that obtained with $L = 4$. There is again a smooth reduction of the deformation by a factor of 2 when Reynolds number increases from 0 to 500. At higher values of Ca and low values of Re the interface violates at the left end the tangency condition discussed before. Increase of L by additional two units to $L = 8$ increases the deformation again by a factor of 3–4 (see

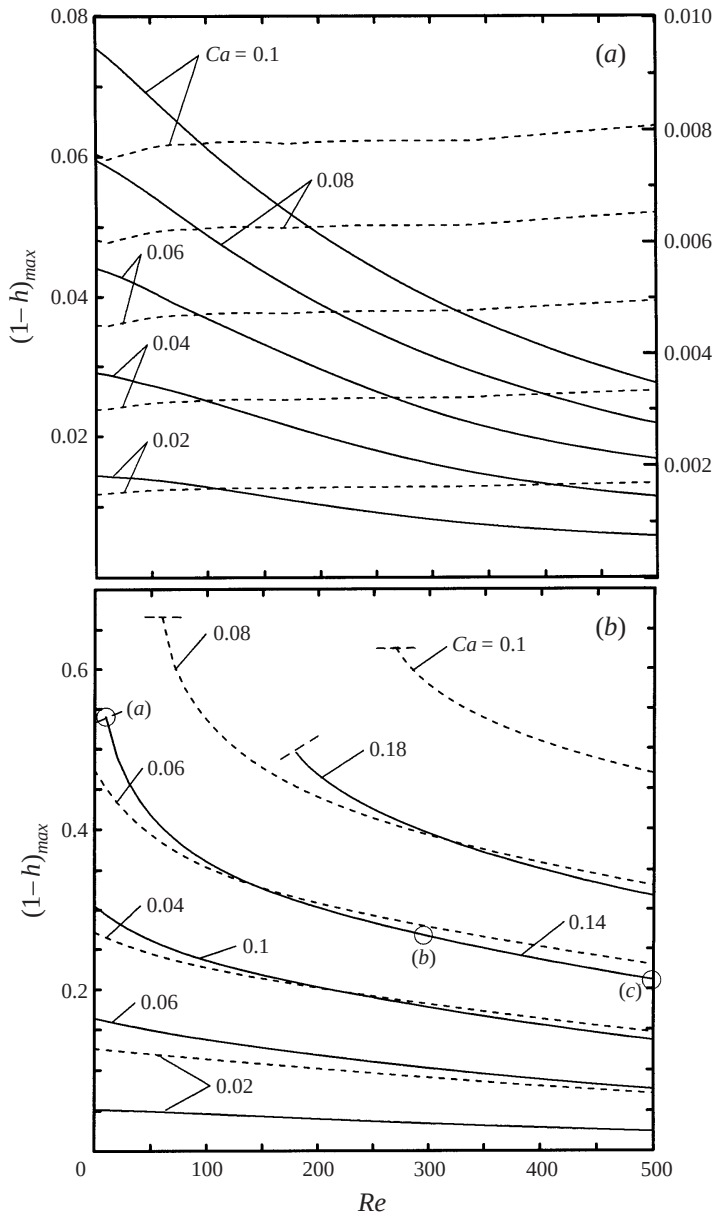

FIGURE 6. The evolution of the maximum of the interface deformation on the left side of the cavity as a function of Reynolds number Re for (a) the cavity lengths $L = 2$ (dotted lines) and $L = 4$ (solid lines); and (b) $L = 6$ (solid lines) and $L = 8$ (dashed lines). The flow and deformation patterns corresponding to points (a–c) are shown in figure 7.

figure 6b). There is a similar reduction of the deformation by a factor of 2 when the Reynolds number increases form $Re = 0$ to 500. The tangency condition is violated for values of Ca smaller by a factor of 2 when compared to the case of $L = 6$. The above results demonstrate that the interface deformation is strongly affected by the cavity length L and rather weakly affected by the Reynolds number Re.

Figure 7 displays the interface and flow pattern as a function of Re for $L = 6$, $Ca = 0.14$. A reduction of the deformation as Re increases is clearly visible. The

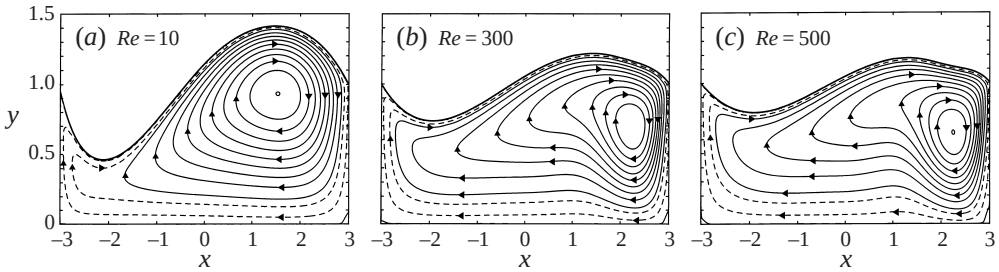

FIGURE 7. The evolution of the flow and deformation patterns as a function of Reynolds number Re for $L = 6$, $Ca = 0.14$: (a–c) respectively correspond to points (a–c) in figure 6(b). Contour lines are shown every 10% of ψ_{max} (solid lines); the dashed lines show 5% and 1% of ψ_{max}. In (a–c) $|\psi_{max}| = 0.5094$, 0.3228, 0.2878 respectively.

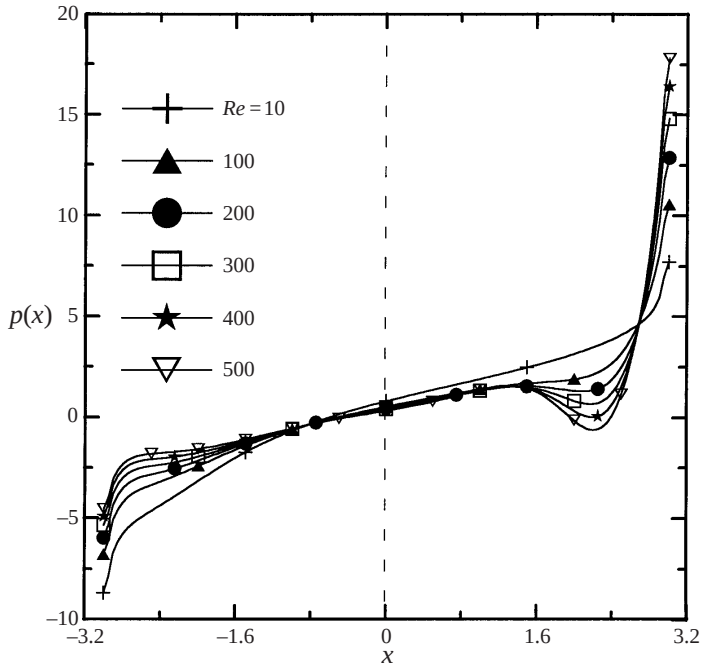

FIGURE 8. Surface pressure distributions as a function of Reynolds number Re for $L = 6$, $Ca = 0.14$.

associated surface pressure distributions, shown in figure 8, are qualitatively similar for all values of Re. They consist of large pressure peaks at the contact points (positive peak at the cold wall, negative peak at the hot wall), an almost identical linear pressure variation away from the contact points, and a local pressure minimum close to the cold wall at a sufficiently high Re. One should keep in mind that the pressure peaks at the contact points are artifacts of the problem formulation leading to pressure divergence at these points. The apparent strength of the divergence on $O(1)$ length scales is influenced by the strength of vorticity near the corners. The cavity may be divided, on the basis of pressure distribution, into three zones, i.e. a central zone (where pressure changes linearly) and two turning zones (attached to the sidewalls). The linearity of pressure in the central zone can be easily explained by

noting similarity with Couette–Poiseuille flow with zero mass flux. Since the liquid is driven to the right along the interface, a pressure gradient must appear to force the liquid back along the bottom of the cavity to guarantee a zero mass flux across the cavity at any fixed x position. It is remarkable that the linearity of the pressure in the central zone can be observed even for large interface deformations. The largest pressure gardient in the central zone is observed at small values of Re (see the curve for $Re = 10$ in figure 8) due to a large viscous friction; the resulting large pressure difference along the cavity length leads to a large interface deformation (figure 7). A further reduction of Re would increase the pressure difference beyond the magnitude that can be supported by the interface, leading to the interface rupture. An increase of Re reduces the pressure gradient (due to the lower friction) and alters the flow field through the increased role played by the inertial effects. Here, the reader may recall that, as Re increases, the centre of the recirculating vortex moves closer to the cold wall and assumes inviscid characteristics. Consequently, the corresponding surface pressure distributions have peaks of smaller magnitude at the hot wall than at the cold wall; the magnitudes of these peaks at the hot wall decrease while those at the cold wall increase with an increase of Re. The pressure peaks by themselves do not play an important role in the interface deformation due to the imposition of the fixed contact points conditions. It is the pressure in the turning zone that directly contributes to the deformation. Pressure in the left (hot) turning zone decreases with Re due to the overall reduction in the strength of convection there. Pressure in the right (cold) turning zone also decreases with Re but due to the formation of an inviscid vortex core, which induces a local pressure minimum (see figure 8). The combined effect of both of the above processes leads to a reduction in the pressure difference between the left and right turning zones and a reduction of the deformation as Re increases (see figure 7). The reader may note the appearance of a small depression in the interface just above the vortex centre at a sufficiently high Re. This depression correlates well with the local pressure minimum (figure 8).

Figure 9 illustrates variations of the interface deformation as a function of the cavity length L. A rapid increase of the deformation as L increases can clearly be seen for all values of Ca and Re considered. All curves have been terminated when the tangency condition at the hot wall was violated. The ends of these curves correspond therefore approximately to the limit points of the system. The form of these curves shows that large deformations always occur, even for very small values of Ca, if the cavity is made sufficiently long.

Figure 10 illustrates evolution of the flow field as a function of L for $Re = 400$, $Ca = 0.04$. The centre of the vortex appears to be attached to the cold wall and moves with it away from the centre as L increases. This vortex remains positioned approximately at the centre of the cavity when $Re = 1$ (not shown). Figure 11 shows the corresponding surface pressure distributions. They consist of a clearly identifiable central zone and two turning zones. The pressure in the central zone has a constant gradient whose magnitude is approximately independent of the cavity length. The length of the central zone increases with L while the size of the turning zones remains approximately constant, with the cold (right) one being noticeably bigger than the hot (left) one. This agrees qualitatively with results of Laure *et al.* (1990) and Ben Hadid & Roux (1992) who observed the turning zone at the cold wall to be much bigger than the turning zone at the hot wall at higher values of Re. This agreement is remarkable in view of the fact that they considered a non-deformable interface while our results include the actual (large) deformations. The reader should, however, keep in mind the fact that the flow structures in the present case are dominated by the

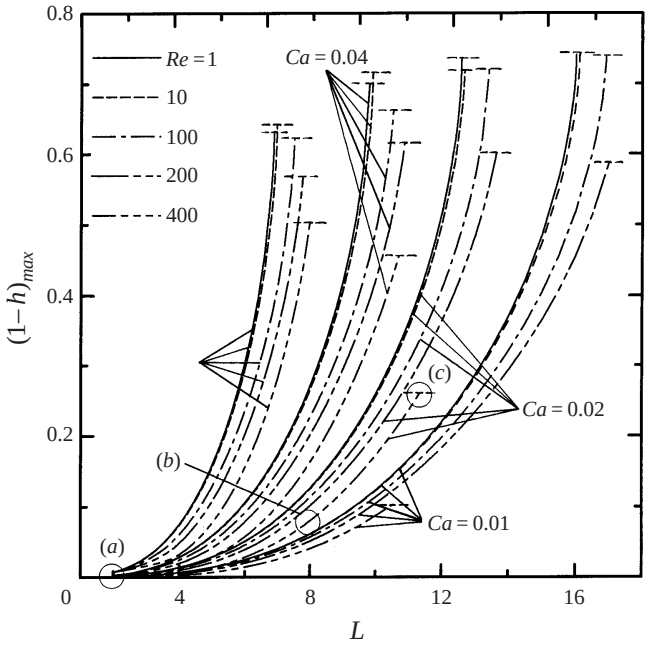

FIGURE 9. The evolution of the maximum of the interface deformation on the left side of the cavity as a function of cavity length L. The flow and deformation patterns corresponding to points (a–c) are shown in figure 10.

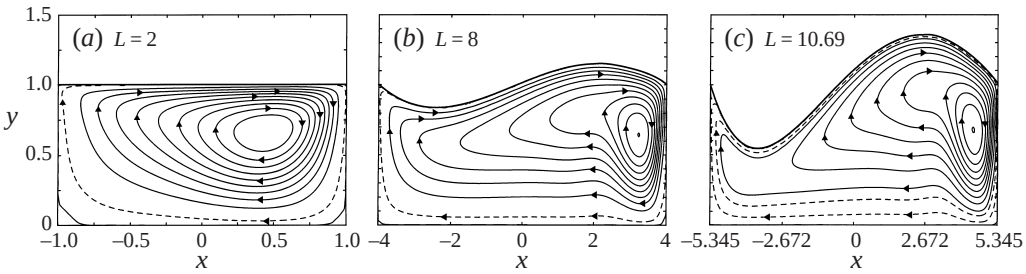

FIGURE 10. The evolution of the flow and deformation patterns as a function of cavity length L for $Re = 400$, $Ca = 0.04$. (a–c) correspond to points (a–c) in figure 9 respectively. Contour lines are shown every 10% of ψ_{max} (solid lines). The dashed line shows 1% of ψ_{max} in (a, b) and 1% and 5% of ψ_{max} in (c). In (a–c) $|\psi_{max}| = 0.0492$, 0.4198, 07172 respectively.

interface shape while in the case of the non-deformable interface considered by Laure *et al.* (1990) and Ben Hadid & Roux (1992) they result from the spatial instability of the basic parallel flow. The magnitude of the apparent pressure peak at the hot (left) wall appears not to change with L, while the one at the cold (right) wall increases noticeably. This increase can be explained by recalling that the centre of the vortex approaches the cold wall as L increases (figure 10). One may note the existence of a local pressure minimum in the cold (right) turning zone associated with the inviscid vortex core.

The magnitude of the interface deformation increases rapidly with L as illustrated in figure 12. For example, the maximum of the deformation on the right side of the cavity assumes the values 0.00327, 0.0132, 0.0283, 0.0563, 0.0964, 0.1485, 0.2126, 0.290,

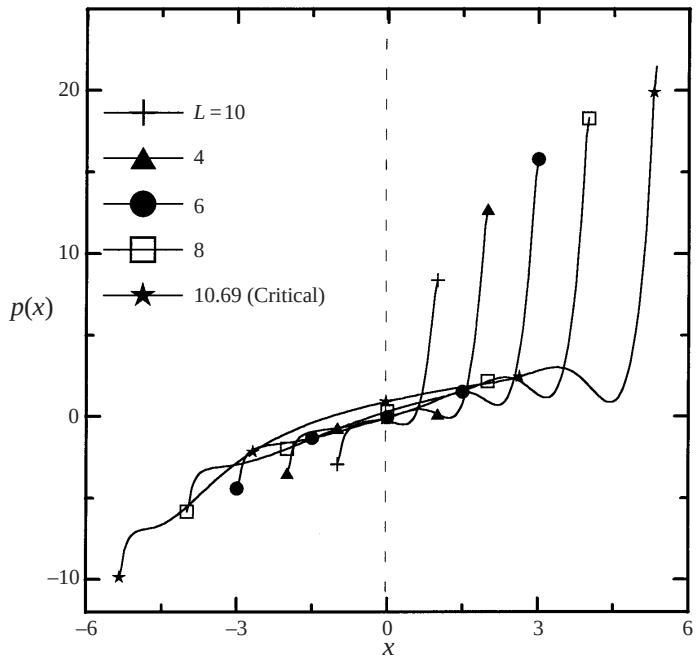

FIGURE 11. Surface pressure distributions as a function of cavity length L for $Re = 400$, $Ca = 0.04$.

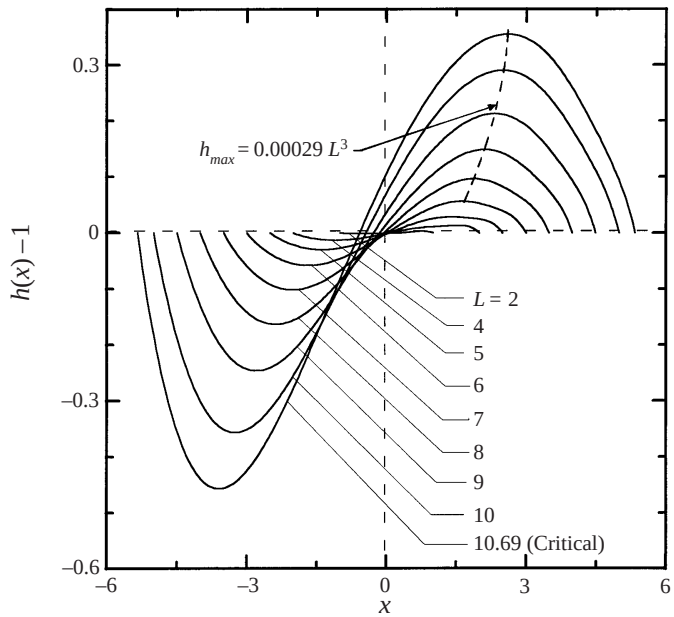

FIGURE 12. The shape of the interface as a function of cavity length L for $Re = 400$, $Ca = 0.04$.

0.03552 for $L = 2, 4, 5, 6, 7, 8, 9, 10, 10.69$ (max), respectively, and correlates well with the third power of L, i.e. $h_{max} = 0.00029L^3$ for $L \in \langle 7, 10 \rangle$. Floryan & Chen (1994) considered the same type of heating and demonstrated, using the small deformation assumption, that for the pressure varying linearly with x in the cavity's central zone, the total pressure variation along the cavity is $O(L)$, and the interface deformation is

dominated by the pressure in the central zone and is $O(L^3)$. Our present results show that these observations remain valid for high deformation and high Reynolds number flow regimes. They underscore the fact that the pressure variations in the turning zones of sufficiently long cavities have a minor influence on the interface deformation.

4.2. *Time-dependent response*

We have described in the previous subsection the steady response of the liquid when the cavity walls are differentially heated with the temperature distribution along the interface described by (4.1). We have determined that the steady-state response exists only for a certain range of parameter values, with the tangency of the interface at the left (hot) contact point being the limiting factor. In the present section, we shall describe what happens outside this range and we shall demonstrate that the tangency condition approximately defines the limit point for the system. We shall also discuss other phenomena associated with different rates of heating. Since the evolution of the system past the limit point could depend on the heating history, we shall consider surface heating in the form

$$T_g(x,t) = g(x)f_i(t), \quad i = 1,2, \tag{4.2a}$$

where $g(x) = -x$ and

$$f_1(t) = \mathscr{H}(t), \qquad f_2(t) = 1 - \exp(-t^2/a). \tag{4.2b,c}$$

Instantaneous heating is described by the Heaviside function $\mathscr{H}(t)$ in (4.2*b*). A variable rate of heating is described by (4.2*c*), where the rate of heating is reduced by increasing the value of the constant a. We shall measure the reduction in the rate of heating by introducing the heating delay time t_D defined as the length of time required to reach 90% of the final surface temperature. For example, for $a = 0.4343$, 10.8574, 43.43, 1086, 4343 the heating delay time t_D is equal to 1, 5, 10, 50, 100 time units, respectively. In our investigations, we shall consider the heating rates changing from $t_D = 0$ (instantaneous heating) to $t_D = O(10^2)$.

We shall begin our discussion by considering the effects of the capillary number Ca on the response of the liquid. Since the form of the unsteady response is a strong function of the Reynolds number Re, we shall discuss each of the selected values of Re separately.

Figure 13 displays the time history of the maximum interface deformation at the left (hot) side of the cavity for $Re = 1$, $L = 6$ resulting from instantaneous heating. One can observe an initial overshoot of the steady state followed by an oscillatory decaying transient for $Ca \leqslant 0.1$. For higher values of Ca (with $Ca \leqslant Ca_{cr}$, $Ca_{cr} = 0.137$), the deformation approaches monotonically the steady state discussed in §4.1. When $Ca > Ca_{cr}$ the deformation continuously increases until the tangency condition at the left (hot) end is violated resulting in the termination of the calculations. The form of the interface evolution suggests that the interface evolves towards creation of a dry spot on the left (hot) sidewall around the contact point. The critical value of the capillary number Ca_{cr}, determined using the tangency condition, defines approximately the limit point of the system beyond which no steady state (corresponding to a continuous interface connecting the specified contact points) exists. The evolution of the interface as well as the flow patterns are shown in figure 14 for $Ca = 0.138$ (which is just above Ca_{cr}).

Figure 15 illustrates the effects of the cavity length L on the interface deformation. It displays the time history of the maximum interface deformation at the left (hot) side of the cavity for $Re = 1$, $Ca = 0.1$ resulting from an instantaneous heating.

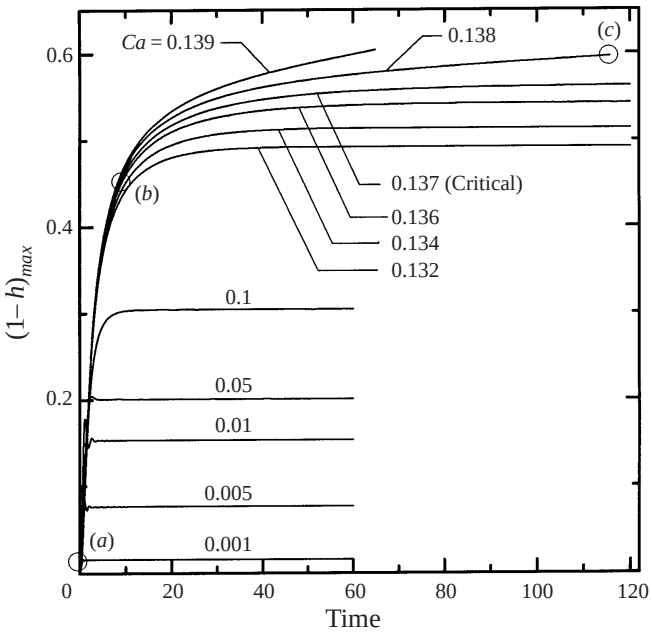

FIGURE 13. The maximum of the interface deformation on the left side of the cavity as a function of time for $Re = 1$, $L = 6$ and instantaneous heating. The flow and deformation patterns corresponding to points (a–c) are shown in figure 14. Deformation levels for $Ca = 0.001$, 0.005 and 0.01 have been multiplied by 6, and for $Ca = 0.05$ by 1.5 for presentation purposes. Curves for other values of Ca present the actual magnitudes of the deformation.

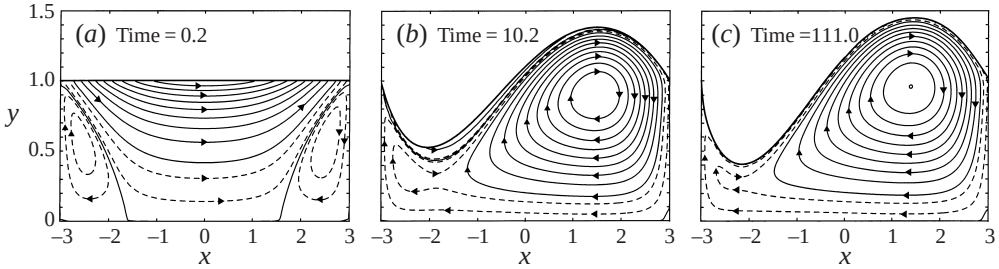

FIGURE 14. The evolution of the flow and deformation patterns as a function of time for $Re = 1$, $L = 6$, $Ca_{cr} = 0.138$ (just above $Ca = 0.137$) and instantaneous heating: (a–c) correspond to points (a–c) in figure 13 respectively. Contour lines are shown every 10% of ψ_{max} (solid lines). Dashed lines show 1% and 5% of ψ_{max}. The second dashed line in the recirculation zones in (a) shows 3% rather than 5% of ψ_{max}. In (a–c) $|\psi_{max}| = 0.0356$, 0.0785, 0.0908 respectively.

One can observe the appearance of an initial overshoot of the steady state and an oscillatory decaying transient for $L \leqslant 4$. When $4 < L \leqslant L_{cr}$ ($L_{cr} = 6.88$), the deformation monotonically approaches the steady state described in §4.1. The critical length L_{cr} corresponds to the maximum length for which the steady state can be determined without violating the tangency condition. When $L > L_{cr}$, the deformation continuously increases until the tangency condition is violated and the calculations are terminated. The form of the interface evolution suggests the eventual formation of a dry spot at the left (hot) wall. The critical cavity length L_{cr} determined using the tangency condition determines approximately the limit point of the system

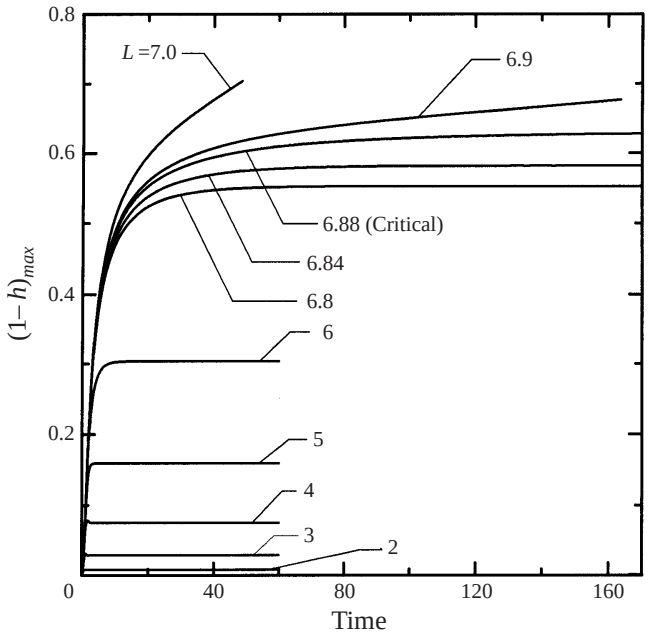

FIGURE 15. The maximum of the interface deformation on the left side of the cavity as a function of time for $Re = 1$, $Ca = 0.1$ and instantaneous heating.

beyond which no steady state (corresponding to a continuous interface connecting the specified contact points) exists.

Figure 16 illustrates the response of the liquid when the Reynolds number is raised to $Re = 30$ with $L = 6$ and with instantaneous heating. When Ca is small enough, an initial overshoot of the steady state gives rise to an oscillatory decaying transient. An increase of the capillary number Ca results in an increase of the amplitude and a decrease of the frequency and the decay rate of the transient. Eventually, at high enough Ca, this transient evolves into a permanent oscillatory state (see, for example, the curve corresponding to $Ca = 0.005$) rather than dying out. Further increase of the capillary number to $Ca \geqslant 0.01$ increases the amplitude and reduces the frequency of the initial transient, but now this transient dies out completely after a sufficiently long time. Still further increase of capillary number to $Ca \geqslant 0.02$ results in a much higher amplitude, a much smaller frequency and a slower decay of the initial transient. In summary, there are two issues of interest, i.e. the form of the final state and the character of the initial transient. As far as the final state is concerned, there is a range of Ca where two such states are possible, i.e. steady state described in § 4.1 and an oscillatory state described above. In this range, it is not possible to reach the steady state with an instantaneous heating. Outside this range, only steady states are possible. As far as the initial transients are concerned, they can (almost instantaneously) easily double the maximum deformation expected under the steady-state conditions and could last for a long time.

Figures 17 and 18 illustrate the response of the system at $Re = 60$ and $Re = 100$, respectively. The qualitative character of the response is the same as in the case of $Re = 30$, i.e. in each case there is a range of values of Ca for which two responses are possible, i.e. a steady and an oscillatory state. An increase of Re leads to a higher amplitude and a smaller frequency and a smaller decay rate of the initial transient.

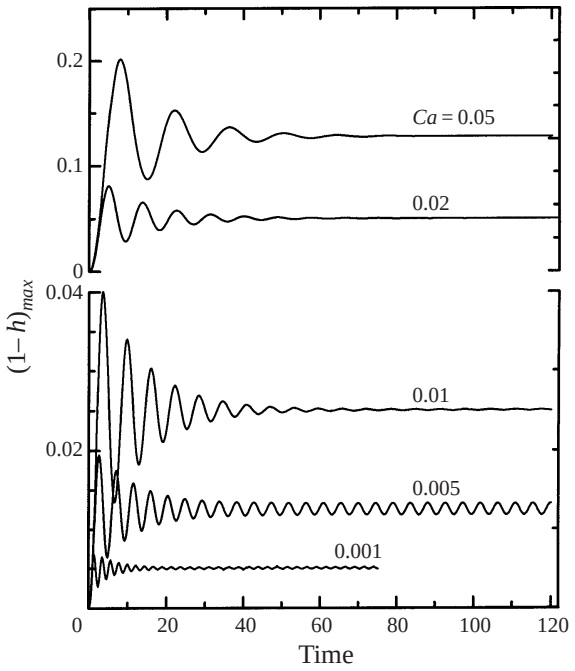

FIGURE 16. The maximum of the interface deformation on the left side of the cavity as a function of time for $Re = 30$, $L = 6$ and instantaneous heating. Deformation levels for $Ca = 0.001$ have been multiplied by 2 for presentation purposes. Curves for other values of Ca present the actual magnitudes of the deformation.

Comparison of figures 16 and 18 demonstrates that it takes more than twice as much time for $Re = 100$ than for $Re = 30$ before the system assumes its permanent state, regardless of whether this state is oscillatory or steady. In the range of Ca where both steady and oscillatory states are admissible, only the oscillatory state can be reached with instantaneous heating. The existence of oscillatory states has been noticed by Chen & Hwu (1993), who considered the cavity of length $L = 2$ and the flows with high values of the Marangoni numbers. They concluded that such states may exist only when the Marangoni number reaches a critical value and that the convective heat transfer effects are essential for their existence. The oscillatory states described here are likely to be driven by a different mechanism which is independent of the convective heat transfer.

The existence of strong initial transients raises the possibility that the fluid may not be able to reach, under some conditions, the steady state without violating the tangency condition. Figure 19 illustrates such a situation. The interface is rather 'soft', $Ca = 0.13$, and instantaneous heating creates a transient deformation which, while not being large in absolute terms, is characterized by very steep slopes at the contact points which violate the tangency condition. The corresponding deformation curve is shown in figure 17. An efficient method for controlling (or eliminating) the initial transients involves reduction in the rate of heating. Figure 17 illustrates the effectiveness of this approach. The rate of heating is described by (4.2*c*). When $Ca = 0.02$, the reduction in the heating rate that corresponds to the delay time $t_D = 40$ completely eliminates the initial transient. When $Ca = 0.13$, the heating with delay time $t_D = 65$ permits reaching the steady state in an almost monotonic fashion and without violating the tangency condition.

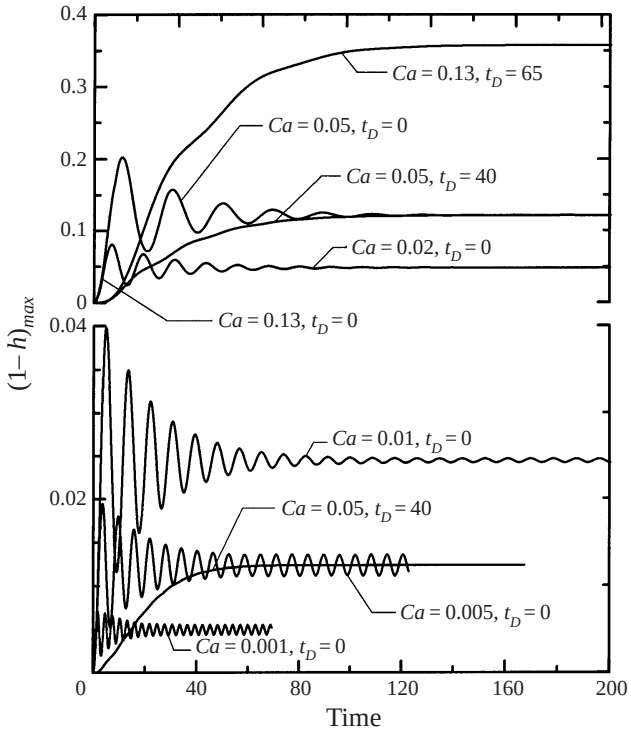

FIGURE 17. The maximum of the interface deformation on the left side of the cavity as a function of time for $Re = 60$, $L = 6$. Delay time $t_D = 0$ corresponds to instantaneous heating. Deformation levels for $Ca = 0.001$ have been multiplied by 2 for presentation purposes. Curves for other values of Ca present the actual magnitudes of the deformation.

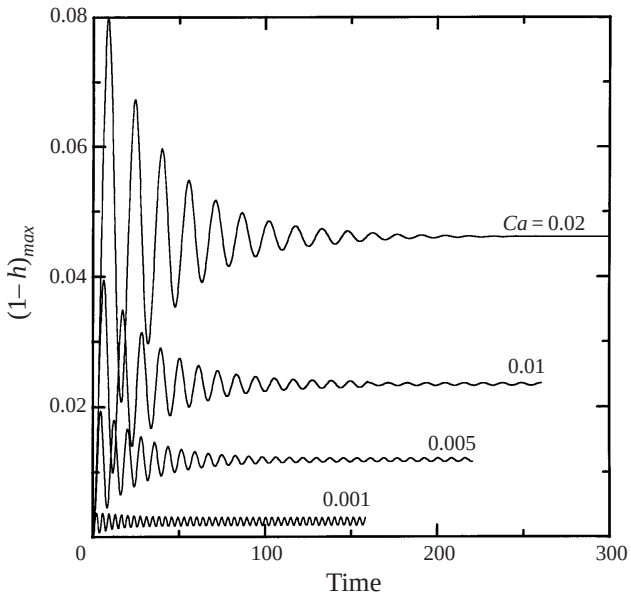

FIGURE 18. The maximum of the interface deformation on the left side of the cavity as a function of time for $Re = 100$, $L = 6$ and instantaneous heating.

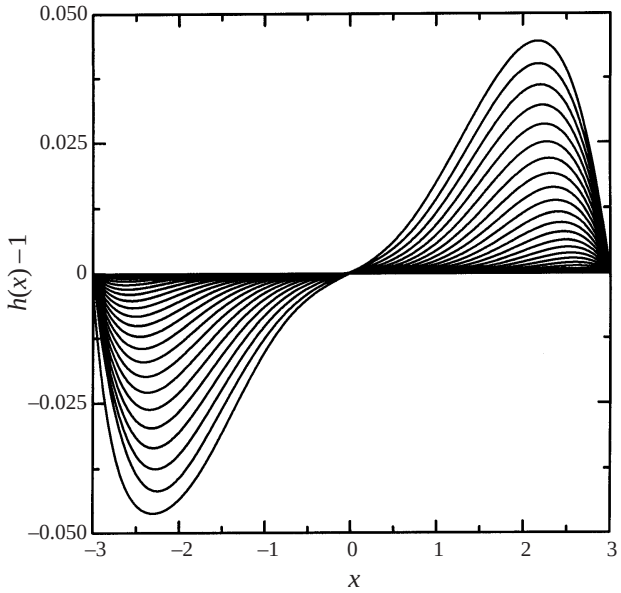

FIGURE 19. The evolution of the interface as a function of time for $Re = 60$, $L = 6$, $Ca = 0.13$ and instantaneous heating. The interface has been plotted at constant step size $\Delta t = 0.2$. The tangency condition is violated at $t = 5.6$.

The existence of two permanent states of motion for a certain range of Ca raises the question of the character of the selection mechanism. Results displayed in figure 17 for $Ca = 0.005$, $Re = 60$, $L = 6$ demonstrate that one may select any of these states by changing the rate of heating, with a sufficiently slow heating favouring the steady state. When the system is already in the steady state, the oscillatory state can be triggered by imposing a large enough disturbance. Figure 20 illustrates such a process. Vorticity at a single grid point located close to the interface around the middle of the cavity ($\xi = 0.005$, $\eta = 0.95$) is disturbed by an amount equal to 1% and 2% of its steady state value. The smaller disturbance initially decays in an oscillatory manner, with the amplitude of the oscillations decreasing at a rate faster than exponential, which suggests a nonlinear process. When the disturbance reaches the magnitude $O(10^{-5})$ the decay becomes purely exponential suggesting a linear stability process. The 2% disturbance grows in an oscillatory manner with the amplitude of the oscillations increasing in a manner suggesting a nonlinear process. The growth reaches a saturation point which corresponds to the permanent oscillatory state discussed before. A 5% disturbance (not shown) decays to the same (oscillatory) state in an oscillatory manner. One can conclude that the steady state is linearly stable in the range of parameters studied, but is nonlinearly unstable with the disturbance threshold being between 1% and 2% of the steady flow values. The instability appears to have a subcritical character and it is possible that the steady state may become linearly unstable at a higher values of Re. This question requires further investigation.

We shall now discuss the characteristics of the oscillatory state. This state consists of a nearly harmonic oscillation, as documented by the frequency spectrum shown in figure 21, and can be represented in the following form:

$$h(\xi, t) = h_{av}(\xi) + h_1(\xi)\cos[f(t - t_o)], \tag{4.3a}$$

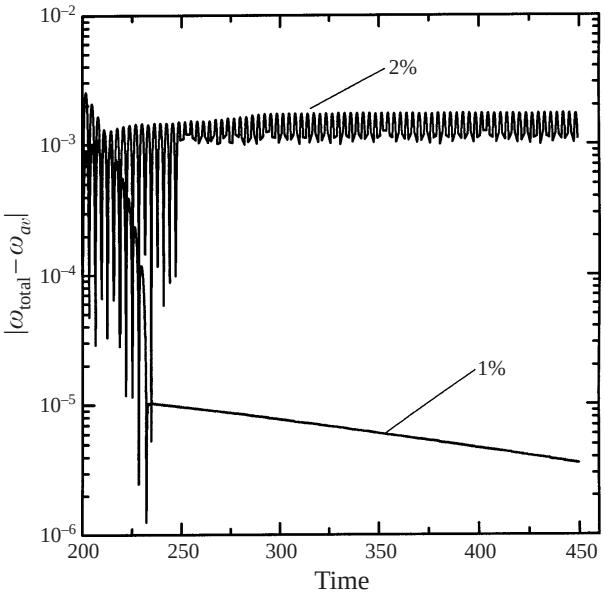

FIGURE 20. The evolution of the vorticity disturbance at a grid point corresponding to $x = \xi = -1.5$, $\eta = 1.0$ as a function of time for $Re = 60$, $Ca = 0.005$, $L = 6$. The initial level of the disturbance is expressed in terms of the percentage of the steady-state vorticity (see the text for a discussion). The downward peaks were eliminated from the 2% curve for $t > 240$ in order to increase the clarity of the figure.

$$p_s(\xi, t) = p_{s,av}(\xi) + p_1(\xi)\cos[f(t - t_o) + \phi], \tag{4.3b}$$

$$\psi(\xi, \eta, t) = \psi_{av}(\xi, \eta) + \psi_1(\xi, \eta)\cos[f(t - t_o) + \phi], \tag{4.3c}$$

where h_{av} denotes the average location of the interface, $p_{s,av}$ denotes the average value of the surface pressure, ψ_{av} stands for the average value of the streamfunction, h_1 denotes the amplitude of the oscillations of the interface, p_1 denotes the amplitude of the surface pressure oscillations, ψ_1 stands for the amplitude of the oscillations of the streamfunction, f denotes the frequency of the oscillations, ϕ denotes the phase shift between the oscillations of the interface and the oscillations of the flow field, and t_o denotes a reference point in time. Figures 22 and 23 display $h_1(\xi)$, $p_1(\xi)$ and $\psi_1(\xi, \eta)$ for $L = 6$, $Re = 60$, $Ca = 0.005$, respectively. The oscillatory state has the form of a sloshing motion (see figure 23) and manifests itself on the interface in the form of a standing wave (see figure 22). One can easily conclude, when looking at figures 22 and 23, that the phase shift between the oscillations of the interface and the flow field must be $\phi = \pi/2$.

The frequency of the oscillations increases with a decrease of Ca and Re, as illustrated in figure 24. The amplitude of the oscillations exhibits a peak at a certain optimum value of the capillary number $Ca = Ca_{opt}$. The value of Ca_{opt} is rather small and it decreases with an increase of Re. For example, the maximum amplitude shifts from $Ca_{opt} \approx 0.005$ at $Re = 30$ to $Ca_{opt} \approx 0.002$ at $Re = 100$. The magnitude of the amplitude at Ca_{opt} is a strong function of Re and it increases approximately by a factor of 3 when Re increases from 30 to 100. Reduction of Ca below the optimum value quickly reduces the amplitude of the oscillations (figure 24) and, in fact, no oscillations can be detected if Ca is sufficiently small. This demonstrates that the appearance of the oscillatory states described here is associated with the

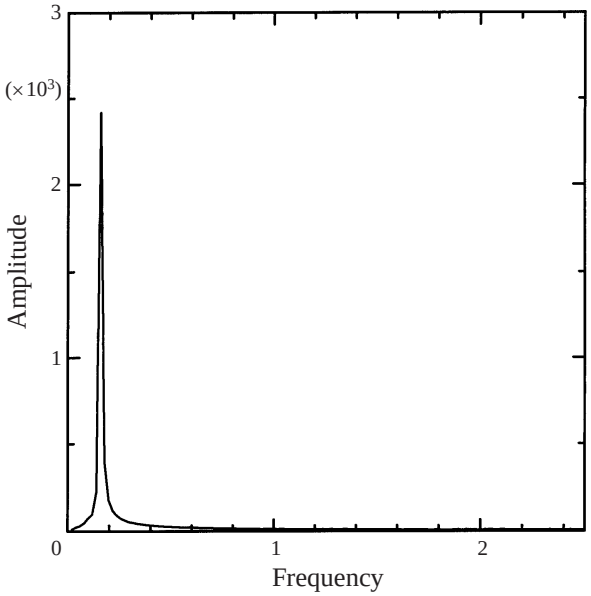

FIGURE 21. The frequency spectrum characterizing the oscillatory motion for $Re = 60$, $Ca = 0.005$, $L = 6$.

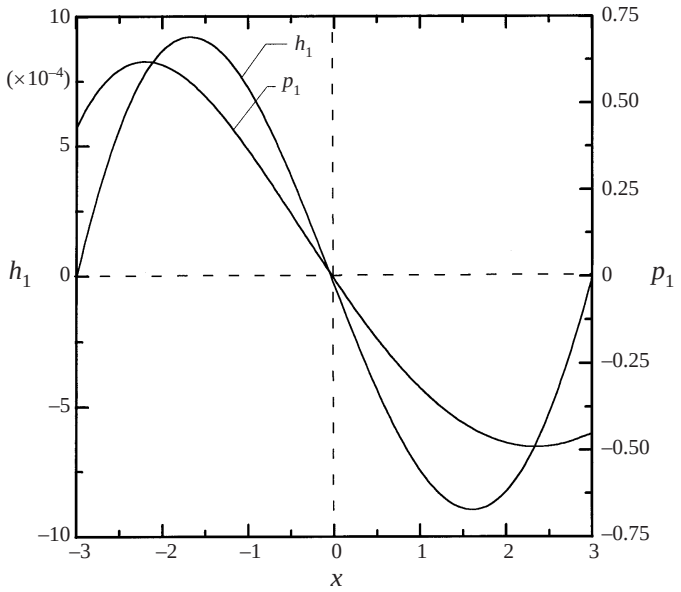

FIGURE 22. The amplitude of the interface oscillations $h_1(x)$ and the surface pressure oscillations $p_1(x)$ for $Re = 60$, $L = 6$, $Ca = 0.005$.

deformability of the interface. Mathematical models of thermocapillary convection that do not properly account for the deformability of the interface are unable to predict the existence of such states. One should keep in mind that oscillatory states driven by mechanisms that are not related to the interface deformability are also possible (Peltier & Biringen 1993; Chen & Hwu 1993). An increase of Ca above Ca_{opt} also decreases the amplitude but at a much smaller rate (this rate is almost linear for $Ca \geqslant 0.015$). The oscillations disappear completely if Ca is sufficiently large.

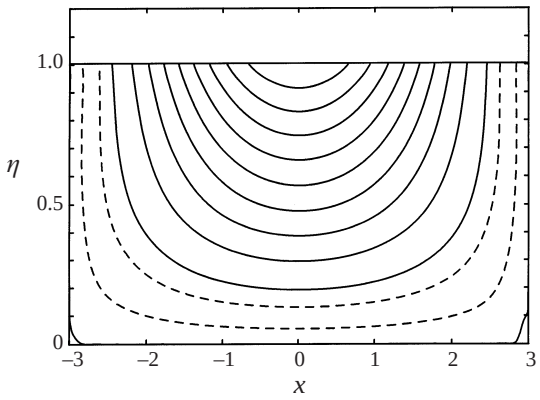

FIGURE 23. The amplitude of the streamfunction of the oscillations $\psi_1(\xi,\eta)$ for $Re = 60$, $L = 6$, $Ca = 0.005$. Contour lines are shown every 10% of ψ_{1max} (solid lines). Dashed lines show 1% and 5% of ψ_{1max}; $|\psi_{1max}| = 0.00345$.

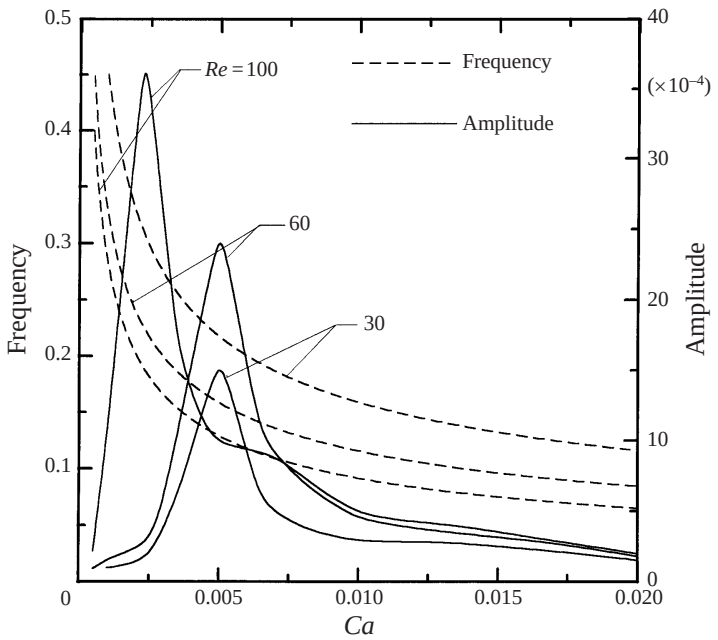

FIGURE 24. The frequency and amplitude of the interface oscillations at $x = \xi = -1.5$ as a function of capillary and Reynolds numbers for the cavity with length $L = 6$.

The oscillatory state strongly depends on the cavity length L. Figure 25 illustrates variations of the amplitude and frequency of oscillations for $Ca = 0.005$. $Re = 60$ as a function of L. One may note the disappearance of the oscillations for a sufficiently short cavity. A qualitatively similar result has been obtained by Peltier & Biringen (1993) who found that an oscillatory state may exist only if the cavity is long enough and the Marangoni number is high enough. Because of the lack of interface deformability and the presence of convective heat transfer effects in their analysis, their oscillations are likely to be driven by a mechanism different from the one responsible for the oscillations discussed here.

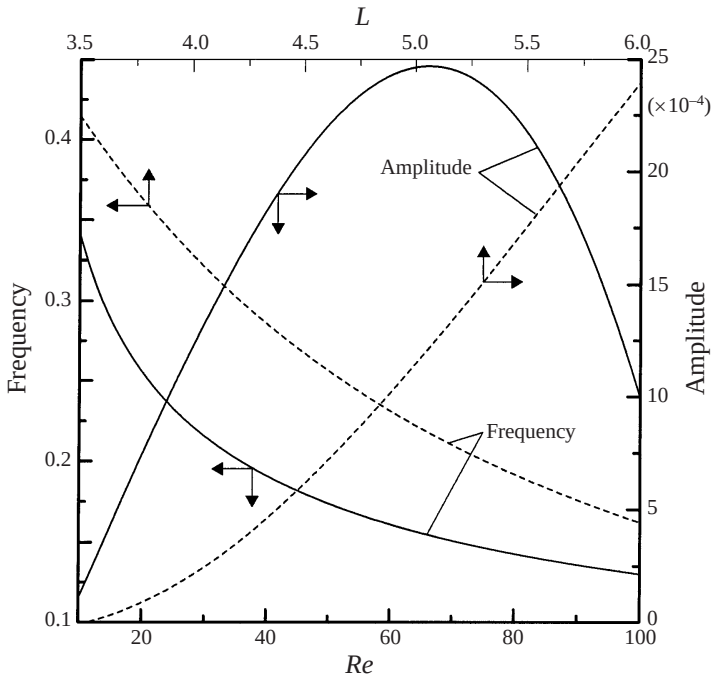

FIGURE 25. The frequency and the amplitude of the interface oscillations at $x = \xi = -1.5$ as a function of cavity length L for $Re = 60$, $Ca = 0.005$ (dashed lines) and as a function of Re for $L = 6$, $Ca = 0.005$ (solid lines).

The effects of the Reynolds number are illustrated in figure 25, displaying the frequency and the amplitude of the oscillations for $L = 6$, $Ca = 0.005$ as a function of Re. A reduction of Re below its critical value ($Re_{cr} \approx 10$ in this particular case) eliminates the oscillation through an increase of viscous dissipation. There is an optimum Re_{opt} which gives rise to the maximum amplitude of the oscillation ($Re_{opt} \approx 65$ in this case). The frequency of the oscillations decreases monotonically as Re increases. The fact that there exist optimum values of Re_{opt} and Ca_{opt} beyond which the amplitude of the oscillations quickly decreases (see figures 24 and 25) suggests that a subtle interplay between the capillary and viscous forces is required to maintain the oscillatory motion.

The above description of the oscillatory states permits one to identify a mechanism responsible for their generation. Surface force (due to the thermocapillary effect) applied to the stagnant liquid pulls this liquid toward the cold (right) wall. When this pull is too strong (or when the fluid inertia is too high), the liquid overshoots the steady equilibrium state resulting in an additional deformation of the interface. The interface acts as a 'spring'; it generates a restoring force by increasing capillary pressure that is proportional to the additional deformation. The restoring force pushes liquid back towards the hot (left) wall. If the restoring force is too high, the liquid overshoots the equilibrium position at the left end and a restoring force with an opposite direction (generated by the interface deformation) appears and forces the liquid to flow back. As a result, one gets the sloshing motion illustrated in figure 22, with the energy being stored and released by the free-surface 'spring'. When the interface in stiffer (smaller Ca; stiffer 'spring'), the frequency of the motion increases (see figure 23). For high enough stiffness (small enough Ca) the initial pull (maximum

pull corresponds to instantaneous heating) is too weak to force the liquid beyond the steady equilibrium position and thus no oscillations result. For high enough Ca (soft interface; soft 'spring') the initial pull creates a large overshoot of the steady equilibrium. Since the restoring force is much weaker, the liquid is gently pushed back toward its equilibrium position and the transient motion dies out after a few oscillations due to dissipation. When Re is small enough, dissipation prevents the appearance of the oscillations. When the initial pull is weakened (by reducing the rate of heating), the oscillatory motion is not triggered. It appears that the oscillatory motion may exist only for a certain stiffness of the interface (as measured by Ca) and that it has to be triggered by a large enough disturbance (in the range of parameters studied) so that the nonlinear properties of the restoring force come into play, with the thermocapillary shear being the energy source.

5. Conclusions

We have investigated Marangoni convection in a cavity with differentially heated sidewalls, including complete interface deformation effects. Detailed results were presented for the case of Marangoni number $Ma = 0$ (dominant conductive heat transport; Pandtl number $Pr = 0$) and Biot number $Bi = \infty$ (very high heat transfer coefficient at the interface).

The results show that steady convection exists only for Reynolds numbers Re larger than, and for capillary numbers Ca and cavity lengths L smaller than, certain critical values. The critical values Re_{cr}, Ca_{cr} and L_{cr} are mutually dependent. When any of Re, Ca or L approaches its respective critical value, the magnitude of the interface deformation increases rapidly, with the interface evolving (as a function of this particular parameter) towards becoming tangential to the hot wall. Such a shape of the interface implies formation of a dryout at the sidewall when any of Re, Ca, or L passes its respective critical value. The critical values of Re, Ca and L were determined using the tangency condition, defined as corresponding to the contact angle between the sidewall and the interface being no less than 5°. It is interesting to find that an increase of Re reduces the interface deformation in the range of parameters studied ($Re < 500$).

The convection pattern consists of a single dominant vortex. When Re increases, the centre of this vortex moves towards the cold wall. When the cavity length increases, the centre of the vortex remains approximately in the middle of the cavity if Re is very small. For high values of Re, the centre of the vortex remains attached to the cold wall and moves away from the centre of the cavity when the cavity length increases. The flow field in the case of longer cavities ($L > 4$) can be divided into a core zone and two turning zones, regardless of the magnitude of the interface deformation. The core zone is characterized by a linear surface pressure distribution. The turning zones at the hot and cold walls exhibit different structures, with the differences easily visible at higher values of Re. For such cases the vortex core, which is located next to the cold wall, attains inviscid characteristics creating a local pressure minimum and a local depression in the interface.

Unsteady analysis shows that the response of the liquid depends on the rate of heating. For Re, Ca and L outside the ranges limited by the critical values Re_{cr}, Ca_{cr}, L_{cr}, the deformation of the interface increases continuously in time from the moment of application of the heating until the tangency condition becomes violated. This shows that Re_{cr}, Ca_{cr}, L_{cr} define the limit points for the flow system. The location of limit points in the parameter space is sensitive to the rate of heating for a certain

range of parameters. The presence of very strong transient effects is responsible for this sensitivity. These transients can be effectively controlled by reducing the rate of heating.

Multiple, i.e. steady and oscillatory, states have been found in a certain range of *Re*, *Ca* and *L*. The oscillatory state has the form of a simple harmonic sloshing motion. It can exist only when the cavity length is greater than a certain critical length, and its amplitude increases with an increase of *L*. The oscillatory state may appear only when the interface is permitted to deform. Its amplitude is a function of Reynolds and capillary numbers, and reaches a maximum for certain optimum values of *Re* and *Ca*. It has been shown that, in the range of parameters studied where multiple states are possible, the steady state is linearly stable. Transition between the steady and the oscillatory states involves a nonlinear instability process. The oscillatory states can be avoided by heating the liquid at a sufficiently small rate.

This work was supported by the NSERC of Canada.

REFERENCES

Batchelor, G. K. 1956 *J. Fluid Mech.* **1**, 177–190.
Ben Hadid, H. & Roux, B. 1992 *J. Fluid Mech.* **235**, 1–36.
Carpenter, B. M. & Homsy, G. M. 1990 *Phys. Fluids* **2**, 137–149.
Chen C. & Floryan, J. M. 1994 *J. Comput. Phys.* **111**, 183–193.
Chen, J. C. & Hwu, F. S. 1993 *Intl J. Heat Mass Transfer* **36**, 3743–3749.
Davis, S. H. 1987 *Ann. Rev. Fluid Mech.* **19**, 403–435.
Floryan, J. M. & Chen, C. 1994 *J. Fluid Mech.* **277**, 303–329.
Hamed, M. S. & Floryan, J. M. 1998 *J. Comput. Phys.* **145**, 110–140.
Hamed, M. S. & Floryan, J. M. 2000 *J. Fluid Mech.* **405**, 111–129.
Laure, P., Roux, B. & Ben Hadid, H. 1990 *Phys. Fluids* A **2**, 516–524.
Liakopoulos, A. & Brown, G. W. 1993 In *Surface Tension Driven Flows* (ed. G. P. Neitzel & M. K. Smith). ASME AMD-170. pp. 57–74.
Mundrane, M., Xu, J. & Zebib, A. 1995 *Adv. Space Res.* **16**, 741–753.
Mundrane, M. & Zebib, A. 1995 *J. Thermophys.* **9**, 795–797.
Peltier, L. J. & Biringen, S. 1993 *J. Fluid Mech.* **257**, 339–357.
Sen, A. K. 1986 *Phys. Fluids* **29**, 3881–3883.
Sen, A. K. & Davis, S. H. 1982 *J. Fluid Mech.* **121**, 163–186.
Zebib, A., Homsy, G. M. & Meiburg, E. 1985 *Phys. Fluids* **28**, 3467–3476.